General Disclaimer

One or more of the Following Statements may affect this Document

- This document has been reproduced from the best copy furnished by the organizational source. It is being released in the interest of making available as much information as possible.

- This document may contain data, which exceeds the sheet parameters. It was furnished in this condition by the organizational source and is the best copy available.

- This document may contain tone-on-tone or color graphs, charts and/or pictures, which have been reproduced in black and white.

- This document is paginated as submitted by the original source.

- Portions of this document are not fully legible due to the historical nature of some of the material. However, it is the best reproduction available from the original submission.

Report 84-3

October 1984

THEORETICAL DEVELOPMENT OF MONTE CARLO CODES FOR MODELING CUMULUS CLOUD FIELDS

By: Ronald M. Welch

Final Report for FY1984:

National Aeronautic and Space
Administration
Langley Research Center
Hampton, VA 23665

Grant No. NAG-1-307

Institute of Atmospheric Sciences

South Dakota School of Mines and Technology

Rapid City, South Dakota 57701-3995

During the last two years there has been much activity and discussion at scientific meetings associated with the International Satellite Cloud Climatology Project (ISCCP). The meteorological community is focusing considerable effort towards the goal of more complete understanding of the effects of clouds upon global and regional radiation budgets. The First ISCCP Regional Experiment (FIRE) workshop defined essential research efforts required to accomplish this goal. An important component of this research plan is the modeling and parameterization of stratocumulus cloud fields.

Consistent with this goal, the present investigation has been oriented towards the development of accurate stratocumulus cloud parameterization for use in stratocumulus cloud field studies. One aspect of this study has been the expression of the radiative properties of broken cloudiness in terms of the better understood horizontally homogeneous plane-parallel values. This type of approach is designed to facilitate the utlization of these results by GCM's and climate models. In particular, cloud liquid water is held constant as cloud shape and cloud cover is varied. This is important since GCM's predict only cloud amount and liquid water content. Only in this way can differences in cloud shape be compared and related back to the predicted values supplied by GCM's.

The proximity of neighboring clouds in a cumulus cloud field significantly alters cloud field radiance through cloud-cloud photon interactions and by shading. Previous studies of cloud field radiative properties have made one or more of the following assumptions: (1) isotropic radiation from cloud sides, (2) neglect of multiple scattering of radiation between clouds, and (3) lack of shading by neighboring clouds. In contrast, the present study makes none of these approximations, but rather uses the Monte Carlo method to simulate cloud field radiative properties exactly.

The supporting paper, "Stratocumulus Cloud Field Reflected Fluxes: The Effect of Cloud Shape" by Welch and Wielicki has been accepted for publication in the Journal of the Atmospheric Sciences (November or December, 1984). Of particular note is the fact that cloud shape has been shown to be a variable as important as cloud optical density and cloud aspect ratio in determining the cloud field radiative properties. The size and shapes of gaps between clouds determines such behavior. This is because clouds have an anisotropic intensity pattern out the cloud sides and because elongated cusp-like regions between clouds are efficient at allowing photons to propagate to the ground without interaction with neighboring clouds.

A recent paper by Harshvardhan and Thomas (1984), published in the 20 August edition of the Journal of Geophysical Research, presented a parameterization scheme for a cloud field composed of two-dimensional bar-clouds. The enclosed paper by Welch and Wielicki generates the three-dimensional version of this technique.

An analysis of this parameterization scheme shows that it rapidly decreases in accuracy for solar zenith angles deviating from $\theta_0 = 60°$. This method also is limited to optically thick clouds, $\tau \geq 10\text{-}20$. The present study has been succesful finding a new parameterization scheme that is accurate for solar zenith angles ranging from $\theta_0 = 0°$ to $82°$ and for all cloud optical depths. The method is the result of a detailed examination of the radiation patterns exiting the cloud sides. Final calculations are in progress, and a paper describing this parameterization scheme is expected to be submitted for publication by the end of the year.

A Monte Carlo scheme including surface albedo also is close to completion. However, this aspect of the study has been downgraded in priority in order to complete the above parameterization scheme. Considerably more effort will be required before the parameterization of surface reflection is accomplished.

STRATOCUMULUS CLOUD FIELD REFLECTED FLUXES:

THE EFFECT OF CLOUD SHAPE

by

R. M. Welch

Institute of Atmospheric Sciences

South Dakota School of Mines and Technology

Rapid City, South Dakota 57701-3995

and

B. A. Wielicki

Atmospheric Sciences Division

NASA Langley Research Center

Hampton, Virginia 23665

ABSTRACT

Reflected fluxes are calculated for stratocumulus cloud fields as a function of sky cover, cloud aspect ratio, and cloud shape. Cloud liquid water volume is held invariant as cloud shape is varied so that the results can be utilized more effectively by GCM and climate models.

Of particular significance is the magnitude of the reflected flux differences between broken and plane-parallel cloudiness. On the basis of required accuracy in the Earth Radiation Budget Experiment (ERBE) program, an order of magnitude value of 10 W m^{-2} is used to estimate "significant differences" between plane-parallel and broken cloudiness. This limit is exceeded for cloud covers between 10% and 90%, indicating that plane-parallel calculations are not satisfactory at most values of cloud cover. The choice of cloud shape also leads to large differences in reflected fluxes. These differences may be traced to the anisotropic intensity pattern out the cloud sides, to the size and shape of the "holes" between clouds, and to variations in cloud area as viewed from the solar direction.

An empirical relationship for effective cloud cover is given at solar zenith angle of $\theta = 60°$. This relationship allows for the relatively accurate ($\Delta F = 10 - 15$ W m^{-2}) computation of broken cloud field reflected fluxes from plane-parallel calculations. Although the present parameterization is limited to solar zenith angles near $\theta = 60°$, this is an indication that further work may lead to reasonably accurate estimates of broken cloud field radiative properties using modified plane-parallel calculations, irrespective of assumed cloud shape.

1. Introduction

The state-of-the-art of cloud modeling in general circulation models (GCMs) is prediction of cloud liquid water content and cloud fraction. Parameterizations using relative humidity and/or vertical velocity were derived by Kasahara and Washington (1971). More recent improvements are typified by Slingo (1980) and Donner et al. (1982) for convective clouds, and by Ramanathan et al. (1983) for cirrus. Given the occurrence of cloud in a GCM grid box and atmospheric layer, the radiative properties of clouds are predicted using horizontally homogeneous plane-parallel radiation codes. A number of radiation column models of varying sophistication have been developed (Geleyn and Hollingsworth, 1979; Fouquart and Bonnel, 1980; Hense et al., 1982; Zdunkowski et al., 1982; Wiscombe et al., 1984), some of which attempt to include multi-layer broken cloudiness. However, comparisons of the radiative output of a large scale atmospheric model with satellite measurements (Geleyn et al., 1982) show a number of weaknesses in current radiation schemes, especially for cloud parameterizations.

Each of the above techniques for modeling cloud radiation is based upon plane-parallel assumptions, whereas satellite images show that a large proportion, if not the majority, of cloud systems are composed of broken cloudiness. Studies by McKee and Cox (1974), Davies (1978), Aida (1977), and Harshvardhan (1982) clearly show that broken cloudiness is characterized by radiation fields quite different from their plane-parallel counterparts. In recognition of these and similar concerns, cloud climatology programs such as the International Satellite Cloud

Climatology Project (ISCCP) and the First ISCCP Regional Experiment (FIRE) are devoted to improving cloud parameter statistics such as cloud cover, cloud top height, etc. In addition, so as to make these results more applicable to modeling efforts, these programs also are aimed at expressing the radiative properties of broken cloudiness in terms of plane-parallel values, adjusted by as yet undefined scale factors (Rossow et al., 1984).

Early attempts to define the properties of broken cloudiness have relied upon the radiative characteristics of individual cloud elements (Busygin et al., 1973; McKee and Cox, 1974; and others). Present efforts now have shifted to the modeling and prediction of the radiative properties of cloud fields. However, parameterizations need to be developed in a way which facilitates their utilization by GCM's and climate models. In the present study, cloud liquid water is held constant as cloud shape is varied. Differences in cloud shape then can be compared and related back to the predicted values supplied by GCM's.

Preliminary attempts to model cloud field radiative properties by Busygin et al. (1973) and Welch and Zdunkowski (1981a,b) did not include cloud-cloud interactions, although Aida (1977) included first order effects. However, the proximity of neighboring clouds significantly alters cloud field radiance through cloud-cloud interactions and shading. Investigations of radiative interactions based upon clouds of identical size and shape have been reported by Aida (1976, 1977), Gube et al. (1980), Bradley (1981), Harshvardhan (1982), Weinman and Harshvardhan (1982), and Claussen (1982). Differences between these

studies are attributed primarily to the various approximations used: (1) isotropic radiation from cloud sides; (2) neglect of multiple scattering of radiation between clouds; and (3) lack of shading by neighboring clouds. In contrast, the present study eliminates these approximations.

The question is raised as to what degree cloud shape and cloud field arrangement are important variables in determining cloud field albedos. In particular, for broken cloudiness does albedo tend uniformly towards the plane-parallel results as cloud amount is increased? Or, can fields of almost overcast clouds have significantly different radiative properties from those of the plane-parallel variety? Such questions are important both for modeling considerations and to the ISCCP and FIRE field programs. The present study seeks to provide a first look at these questions by examining the effect of cloud shape upon cloud radiative interactions and by determining those values of sky cover for which the simpler plane-parallel radiation calculations are adequate and those values for which the more complicated broken cloudiness computations are required.

2. Method of calculation

The Monte Carlo method is based upon the Markov chain formulism by which the interaction of a photon with cloud droplets is independent of all previous interactions. This is a stochastic process for which the probabilities associated with each scattering event are a function only of the present state of a photon packet and not its history (Marchuk et al., 1980). With respect to radiative cloud computations,

photon packets are traced through atmosphere and cloud, accounting for both absorption and scattering along the path, until they either reach the earth's surface or are returned to space.

a. Monte Carlo computations

The Monte Carlo method simulates the photon path; between the $(i-1)^{th}$ and the i^{th} scattering event, the photon travels distance S_i, as determined from the solution:

$$T_i = e^{-t_i} \tag{1}$$

$$t_i = (\sum_j \beta_j S_j)_i \tag{2}$$

$$S_i = (\sum_j S_j)_i \tag{3}$$

where T_i is the transmissivity (randomly chosen between 0 and 1), t_i is the optical path for this event, β_j is the volume extinction coefficient of the j^{th} cloud subregion, and S_j is the distance traveled through the j^{th} subregion. Generally, cloud subregions are partitioned into cubic and rectangular shapes for ease of computation. Within each subregion or "box," cloud attenuation coefficients and phase functions are assumed to be uniform. However, these values may vary from box to box.

After traveling distance S_i, scattering initiates a new direction of travel. A new azimuthal angle γ is randomly assigned with value between 0 and 2π, representing rotation of the x-y axes about the axis z. A second rotation α of the y-z axes about the axis x' is found from the solution to

$$\frac{\int_0^{\alpha} P(\alpha') \sin \alpha' d\alpha'}{\int_0^{\pi} P(\alpha') \sin \alpha' d\alpha'} = Q(\alpha) \qquad (4)$$

where $P(\alpha)$ is the scattering function; $Q(\alpha)$ is randomly assigned a value between 0 and 1, and then the value of α is determined.

The photon path is traced until it exits a cloud side. Outside of the cloud, the photon is followed until it either reaches the ground, enters a neighboring cloud, or is traced to the top of the earth's atmosphere. Cloud exit position (x,y,z) and exit angles (θ,ϕ) for each photon are saved for subsequent analysis.

b. Cloud-cloud interactions

The cloud field is assumed to be composed of clouds of identical diameter (D), shape, and internal optical properties, as discussed in Section 3. Spacing between cloud centers (S) is varied to simulate cloud cover (N), where

$$N = (D/S)^2 \quad \text{(cubic clouds)} \qquad (5)$$

Table 1 shows values of (S/D) used in this study.

A photon packet exiting from a cloud side may experience multiple scatterings between clouds, entering the sides of neighboring clouds before finally reaching the ground or reaching the top of the atmosphere. In this case, the photon is reentered into the original cloud at the equivalent position and angle, as shown by primes in Fig. 1 (i.e., periodic boundary conditions).

c. Cloud geometry

Figure 2 shows the cloud geometries assumed in this investigation. In addition to the cubic shape, the convex geometries of hemispheres, cylinders, and capped cylinders (cylindrically shaped bases with hemispherically shaped tops) are included.

It should be noted that the cloud convex geometry is defined by the appropriate functions; it is not approximated by smaller rectangular-shaped boxes. The intersection of a straight line (i.e., the photon path) with the convex function allows the entry and exit points for each photon to be precisely located.

Figure 3 shows an example of a cloud field composed of convex shaped clouds of diameter D, and with spacing S between cloud centers. Cloud cover N for these clouds is given by

$$N = \pi/4 \ (D/S)^2 \tag{6}$$

for the array shown in Fig. 3a. Table 1 shows the values of cloud cover N as a function of cloud separation (S/D).

The hexagonal cloud field pattern shown in Fig. 3b occasionally is observed in nature. In this case, cloud cover is given by

$$N = (\pi\sqrt{3}/6)(D/S)^2 \tag{7}$$

with values given in Table 2.

d. Shadowing

Mutual shadowing (Fig. 4) occurs for cubic and cylindrically shaped clouds for which cloud spacing in the plane of the sun is

$$S/D < 1 + H/D \tan \theta_o \quad . \tag{8}$$

The shadow region for the convex shaped clouds is not as extensive as for the cubic clouds. The point P shown in Fig. 4b, at a distance Z from cloud top and at a distance x from cloud center, is shaded by its neighbor for

$$z \tan \theta_o > S - (D^2 - 4x^2)^{1/2} \quad . \tag{9}$$

Expressions for cloud shadowing using hemispherical (SPH) and capped cylinder (SPHCYL) clouds are more complicated and are not given here. Nevertheless, similar conditions apply.

e. Effective cloud fraction

In order to be incorporated into GCM and climate models, cloud field radiation budgets need to be expressed in some easily parameterized form. Therefore, the radiative properties of the cloud field are expressed in terms of the better understood plane-parallel values, i.e., $F_{cf}(N)/F_{pp}(N)$, where $F_{cf}(N)$ is cloud field flux at sky cover N and $F_{pp}(N)$ is the plane-parallel flux at the same value of cloud cover:

$$F_{pp}(N) = N\, F_{pp}(100\%) \quad . \tag{10}$$

The ratio $F_{cf}(N)/F_{pp}(N)$ is equivalent to the ratio N_e/N described by Sparrow and Cess (1978) and Weinman and Harshvardhan (1982), where N_e is defined as the equivalent cloud fraction of a plane-parallel cloud of the same optical thickness which produces the same flux as from the finite cloud array. Analytical expressions for $F_{cf}(N)/F_{pp}(N)$

appropriate to arrays of cubic and cylindrically shaped clouds are given in Appendix A.

f. Reflected flux

With respect to using the results (Sec. 3) in GCM and climate models, one of the key quantities is the difference in energy reflected back to space. The difference between broken cloud and plane-parallel reflected fluxes is given by

$$\Delta F = F_{cf}(N) - F_{pp}(N) \quad , \tag{11}$$

expressed in W m^{-2}. Using Appendix A, this flux difference may be expressed as

$$\Delta F = F_0 \mu_0 N [(1+H/D \tan \theta_0) R_c - R_{pp}] \tag{12}$$

where F_0 is incident solar flux, μ_0 is the cosine of the solar zenith angle θ_0, R_{pp} is plane-parallel albedo, and R_c is cloud albedo, defined as the fraction of photons intercepted by the cloud (top and sides) which are reflected back to space. An equivalent expression is

$$\Delta F = F_0 \mu_0 R_{pp} N [F_{cf}(N)/F_{pp}(N) - 1] \quad . \tag{13}$$

The above results are valid only for non-absorbing regions of the solar spectrum. A complete integration across the solar spectrum is beyond the scope of the present investigation. However, a first-order correction of Eq. (13), including the effects of absorption and Rayleigh scattering, is made below. First, Rayleigh scattering is approximated following Lacis and Hansen (1974). Their parameterization,

accurate to 1%, provides estimates of Rayleigh scattering, R_R, of 3.8% at solar zenith angle $\theta_0=0°$ and 6.6% at $\theta_0=60°$.

Second, absorption is estimated from the results of Davis et al. (1979), who calculated the distribution of solar absorption in finite clouds based upon the partitioning of the solar spectrum into three regions. The optical constants, water vapor absorption coefficients and energy for each region are given by Welch et al (1976). The tropical atmosphere given by McClatchey et al. (1971) was used, with the top of the atmosphere assumed at 15 km. Davis et al. found values of absorption, A_b, above their cloud 630 m thick of 299 W m^{-2} at $\theta_0=0°$ and 174 W m^{-2} at $\theta_0=60°$. These values are nearly independent of cloud optical thickness.

Using the above values, Eq. (13) becomes

$$\Delta F = [F_{o}\mu_{o}(1-R_R)-A_b]R_{pp}N[F_{cf}(N)/F_{pp}(N) - 1] \quad . \tag{14}$$

g. Error analysis

Using the Gaussian approximation to the binomial distribution of N_p photons, where P is the probability a photon is reflected back to space and (1-P) is the probability that a photon is transmitted (or absorbed), then the standard deviation for a determination of reflectance P is given by

$$\sigma_p = [P(1-P)N_p^{-1}]^{1/2} \quad . \tag{15}$$

For the present calculations, cloud field reflectance varies from about P = 0.6 to about P = 0.85. For the constant value of N_p = 5000 photons assumed in these computations, σ_p ranges from 0.005 to 0.007.

The corresponding standard deviation for $F_{cf}(N)/F_{pp}(N)$ is given by

$$\sigma_f = \sigma_p \, R_{pp}^{-1} \, A_C(\theta_o)/A \qquad (16)$$

where $A_C(\theta_o)/A$ is given in Appendix A. At solar zenith angle of $\theta_o=0°$, σ_f takes values of 0.006 to 0.009, or less than 1%.

Similarly, the standard deviation for ΔF (Sec. 2f) in which clouds do not shade their neighbors is

$$\sigma_{\Delta F} = (F_o\mu_o)' N \, (1+H/D \tan \theta_o) \, \sigma_p \quad , \qquad (17)$$

where $(F_o\mu_o)' = F_o\mu_o(1-R_R)-A_b$ is corrected for Rayleigh scattering and absorption (Sec. 2f). Note that the error in ΔF for unshaded clouds is proportional to cloud cover N. For shaded clouds,

$$\sigma_{\Delta F} = (F_o\mu_o)' N^{1/2} \, \sigma_p \quad , \qquad (18)$$

with the error in ΔF proportional to the square root of cloud cover.

Now the largest value of σ_p occurs for P = 0.5, so that

$$\sigma_p < 0.5 \, N_p^{-1/2} \quad . \qquad (19)$$

Using this value, the number of photons necessary to provide a given accuracy $\sigma_{\Delta F}$ can be estimated from

$$N_p = [(F_o\mu_o)' 0.5 \, N_e/\sigma_{\Delta F}]^2 \qquad (20)$$

where, for cubes,

$$N_e = \begin{cases} N(1+H/D \tan \theta_0 & , \quad \text{no shading} \\ N^{1/2} & , \quad \text{shading} \end{cases} \tag{21}$$

Note that Eq. (20) may be expressed as

$$N_p = (\text{signal/noise})^2 \quad , \tag{22}$$

where the signal is the plane-parallel reflected flux calculated on the basis of cloud fraction N_e, and the noise is the uncertainty in ΔF.

3. Results

Stratocumulus cloud fields contain clouds of approximately uniform thickness. In the following results, all clouds are assumed to be 1 km thick, single scattering albedo is taken as $\omega_0 = 0.999$, and the phase function is approximated by the Henyey-Greenstein function with asymmetry factor $g = 0.85$. Clouds within the field are assumed to all be of equal size and shape and to be arrayed in regular patterns of horizontally infinite extent. These assumptions are compatible with earlier studies by Aida (1977), Claussen (1982), and Weinman and Harshvardhan (1982).

Four different cloud shapes are investigated, as shown in Fig. 2. For cubic and cylindrically shaped clouds, the volume extinction coefficient is taken to be $\beta_e = 49$ km^{-1}. This value is chosen in order to compare the present results with previous studies. Cloud diameter is varied, keeping cloud thickness fixed, in order to study the effects of cloud aspect ratio.

Plank (1969) found cloud aspect ratio of unity as an average value for his aircraft observations of cloud fields, but with H/D ranging

between values of about 2 and 1/2. Blackmer and Serebreny (1962) found $H/D < 1$, and Bradley (1981) observed H/D ranging between 0.07 and 3.5 with mean value of 0.73. Finally, Hozumi et al. (1982) found that aspect ratio increased with increasing cloud depth, where $H < 1$ for small clouds ($D < 1$ km), and $H/D > 1$ for large clouds ($D > 3$ km). In the following results, cloud diameter is varied between $D = H/2$ and $D = 2H$ in order to examine the importance of cloud aspect ratio H/D upon cloud field radiative characteristics.

An important aspect of this investigation is the fact that liquid water mass in the cloud field is held constant as cloud shape is varied. For example, consider a GCM which predicts liquid water mass m_ℓ condensed into a given latitude/longitude grid box and vertical layer. Distribution of this liquid water into cloud volume v_{cld} determines the average cloud liquid water content $w_\ell = m_\ell / v_{cld}$. For a given cloud fractional coverage in the layer, cloud volume varies with assumed cloud shape, causing a variation of liquid water content with cloud shape. Assuming a specified cloud droplet distribution, cloud extinction is linearly proportional to liquid water content. Therefore, comparisons of cloud fields of different cloud shapes, normalized to conserve liquid water mass in the cloud field, is accomplished by adjusting cloud extinction coefficient. These values are increased from $\beta_e = 49$ km^{-1} to $\beta_e = 59$ km^{-1} and $\beta_e = 73$ km^{-1} for capped cylinders and hemispheres, respectively.

a. Cubic cloud reflected flux ratios

With few exceptions, previous studies of individual cloud and cloud field radiative properties have been based upon cubic and

rectangular geometries. For the purpose of comparison, this cloud geometry is examined first.

The value of $F_{cf}(N)/F_{pp}(N)$ shown in Fig. 5a for solar angle (θ_o=0°) varies almost linearly with cloud fraction N. The broken cloud field produces cloud radiative flux values which are smaller than the plane-parallel values. For N = 1, sky cover is complete and the plane-parallel limit is reached. Increasing (decreasing) cloud aspect ratio, produced by decreasing (increasing) cloud width, leads to greater (smaller) variations from the plane-parallel values. A physical explanation of why cloud field fluxes $F_{cf}(N)$ vary with aspect ratio for fixed value of sky cover N is deferred to the next section with discussion of cylindrically shaped clouds.

Note that calculations are made at each of the points listed in Table 1, as well as at the shadowing limit. Error bars are small (on the order of 1%) and are omitted from the figures, with the curves smoothed to within these limits. A complete description of the error analysis is given in Section 2g.

Figure 6a shows a comparison of the present results with those of Aida (1977), Claussen (1982), and Weinman and Harshvardhan (1982) for θ_o = 0°. The present values and those given by Aida (1977) are nearly identical. However, Aida included cloud-cloud interactions only from the eight nearest neighbors and allowed only a single photon interaction between clouds. In contrast, the present results include all possible interactions between clouds in the cloud field. The fact that the present values and those given by Aida are nearly identical shows that

first order interactions are adequate in simulating cloud-cloud interactions, at least at solar zenith angle of $\theta_0 = 0°$. Values of $F_{cf}(N)/F_{pp}(N)$ given by Claussen (1982), based upon an approximation which neglected shading, are somewhat larger than the present results. Values given by Weinman and Harshvardhan (1982), based upon the delta-Eddington approximation and assumed diffuse fluxes from the cloud sides are somewhat smaller.

At solar zenith angle of $\theta_0 = 60°$, the stratocumulus field produces flux values in excess of those predicted for the plane-parallel case (Fig. 5b). The largest variations from plane-parallel occur at the shadowing limit. After shadowing occurs, the value of $F_{cf}(N)$ approaches the value $F_{pp}(N)$ as sky cover N is increased. $F_{cf}(N) > F_{pp}(N)$ at $\theta_0 = 60°$ since a large portion of incoming radiation is incident upon the cloud sides, increasing cloud effective area. Increasing cloud aspect ratio produces very large deviations from the plane-parallel limit at small values of sky cover. Maximum values of $F_{cf}(N)/F_{pp}(N)$ of 2.4, 1.7, and 1.4 occur at the shadowing limit for cubes at N = 5%, 13%, and 23% for H/D = 2, 1, 1/2, respectively. For sky cover of $N > 0.3$, cloud aspect ratio has diminishing impact upon the value of $F_{cf}(N)/F_{pp}(N)$; however, at smaller values of N, aspect ratio is the dominant factor determining effective cloud cover.

No intercomparison of results is shown for $\theta_0 = 60°$ in Fig. 6a. Neither Weinman and Harshvardhan (1982) nor Claussen (1982) provide values at this solar zenith angle. Aida (1977) gives a value of 65% for his closely packed 9-cloud model. This value is much less than the 85%

calculated in the present results using Monte Carlo and various plane-parallel methods, indicating that there is an error in his computations. Therefore, at $\theta_0 = 60°$, Aida's results have not been intercompared with the present calculations.

b. Cubic cloud flux differences

For climate models, the key quantity is the difference in radiative flux reflected back to space between broken and plane-parallel clouds. As discussed in Section 2f, a first order correction for absorption and Rayleigh scattering can be made.

However, while it is beyond the scope of the present investigation to directly include absorption for all cloud shapes and aspect ratios, a single computation was made for cubic clouds with H/D = 1. This computation used the same partitioning of the solar spectrum as reported by Davis et al. (1979), but with volume extinction coefficient of $\beta_e = 49$ km^{-1} and cloud thickness of 1 km. Fluxes were normalized to cloud top so as to avoid differences due to absorption above the cloud. Resulting values of $F_{cf}(N)/F_{pp}(N)$ are nearly identical to those shown in Fig. 5a. This is due to the fact that absorption values in plane-parallel and finite clouds are nearly identical, in agreement with Davis et al. (1979). This result provides further justification to the procedure outlined in Section 2f.

The differences between broken cloud and plane-parallel reflected fluxes are computed using Eq. (14) and are given in Fig. 5b. These values of ΔF are calculated using plane-parallel values of cloud reflectance, R_{pp}, of 0.79 at $\theta_0 = 0°$ and 0.85 at $\theta_0 = 60°$. At $\theta_0 = 0°$ and for

cloud cover of 50%, broken cloud fields are darker than their plane-parallel counterparts, with differences ranging from 30 W m^{-2} for clouds with aspect ratio H/D = ½ to about 60 W m^{-2} for H/D = 2 (tall clouds). In contrast, at θ = 60° and for cloud cover of 40 - 50%, broken clouds intercept additional energy through their sides and are brighter than their plane-parallel counterparts. In this range of cloud cover, flux differences, ΔF, range from about 40 W m^{-2} for aspect ratio H/D = ½ to about 60 W m^{-2} for H/D = 2. The errors in this analysis are calculated from Section 2g using Eqs. (17-18). For N = 0.5, errors are about $\sigma_{\Delta F}$ = 5 W m^{-2}. The curves in Fig. 5b are smoothed to within these limits, and the error bars are omitted.

The question arises as to what a significant difference is between broken and plane-parallel cloudiness. For a region 250 km on a side, the Earth Radiation Budget Experiment (ERBE) observational program estimates a required accuracy of between 2 and 14 W m^{-2} (Barkstrom and Hall, 1982) for monthly mean values of reflected solar fluxes. Using 10 W m^{-2} as an order of magnitude for significant differences in reflected fluxes, Fig. 5b suggests that finite cloud and plane-parallel results are significantly different for cloud covers ranging between N = 0.1 and 0.9. While the current study examines these differences for two solar zenith angles, a more complete treatment will require averages over sun angles throughout the day. The present study points out the large potential for such differences.

Figure 6b gives the comparison of ΔF with other studies at θ_0 = 0°. Calculated from the results of Weinman and Harshvardhan (1982), the

maximum difference in fluxes, ΔF, is 30 W m^{-2}, compared to 40 W m^{-2} calculated from Aida (1977) and the present study; Claussen's (1982) calculations result in slightly larger flux differences.

c. Cylindrically shaped clouds

For deep, growing clouds which constituted more than half of his sample, Bradley (1981) found cloud shape to be nearly cylindrical. Figure 7 shows a LANDSAT image of a stratocumulus field with high cloud cover and with close cloud spacings. In many cases shown here, the clouds may be approximated by circular cross-sectional areas. For the sake of intercomparison with cubic clouds, the cloud distribution shown in Fig. 3 is used for most of the results presented in this section. Nevertheless, Fig. 7 suggests that the hexagonal cloud array is more representative for real cloud fields. Results for both the linear and hexagonal arrays are given below.

Figure 8a shows values of $F_{cf}(N)/F_{pp}(N)$ as a function of cloud cover. There are many similarities with the results for cubes shown in Fig. 5, but also notable differences. In particular, for the linear array at closest cloud spacing (N = 0.79), the curves do not tend towards the plane-parallel limit $F_{cf}(1)/F_{pp}(1) = 1$. In order to reach the plane-parallel limit as sky cover is increased, the cylinders must be progressively deformed to fill the holes between the clouds.

In order to gain insight concerning the shape of the curves shown in Figs. 5a and 8a, refer to cloud area ratio $A_C(60°)/A_C(0°)$ as plotted in Fig. A1. Note that the shading limit for cylinders occurs for N = 0.24, 0.11, and 0.06 for cloud aspect ratios of H/D = 1/2, 1, and

2, respectively. At small values of sky cover, before shading occurs, the area ratio has the constant value $(1+H/D \tan \theta_0)$ for cubes, but the larger values of $(1+4 \pi H/D \tan \theta_0)$ for cylinders. Examination of Figs. 1-3, along with simple geometrical analysis, reveals that the curved sides of cylinders produce this larger area ratio. After the shadowing limit is exceeded, the value of area ratio $A_C(60°)/A_C(0°)$ decreases rapidly with increasing value of sky cover. For large values of N, the area ratio varies as N^{-1}.

The increase in values of $F_{cf}(N)/F_{pp}(N)$ at small values of N, up to the shadowing limit, is due to cloud-cloud interactions. However, the decrease in values after the shadowing limit is reached demonstrates the important result that geometrical shadowing effects are dominant over increases due to cloud interactions. Weinman and Harshvardhan (1982) reached a similar conclusion for studies of two-dimensional bar clouds.

Figure 8b shows the corresponding values of ΔF. At $\theta_0 = 60°$, $F_{cf}(N)$ exceeds the plane-parallel value $F_{pp}(N)$ by maximum values of 75 W m^{-2} at sky covers of N = 0.4 - 0.5. These values are about 15 - 30 W m^{-2} larger than corresponding values found for cubes (Fig. 5b). Choice of aspect ratio and cloud array patterns have a relatively small (10-15 W m^{-2}) impact upon the values of ΔF at $\theta_0 = 60°$. Cloud fields composed of cylinders are brighter than those composed of cubes because the cylinders have larger effective areas, as shown in Fig. A1.

The situation is diametrically opposite at $\theta_0 = 0°$, for which case aspect ratio is an extremely important variable. Maximum value of ΔF

increases from 45 W m^{-2} for H/D = 1/2 to about 90 W m^{-2} for H/D = 1 to about 130 W m^{-2} for H/D = 2. These differences are much greater than those predicted for cloud fields composed of cubic geometries. Therefore, for $\theta_0 = 0°$ and for constant value of cloud cover, a cloud field composed of cylinders is considerably darker than one composed of cubes. Differences between cylinders and cubes are smallest for flat clouds (H/D = 1/2) and greatest for tall clouds (H/D = 2).

d. "Holes" between clouds

A discussion of the mechanisms producing the large differences between cubes and cylinders follows. Consider the case of N = 0.7 for which these differences are large. In this instance, cubes have separation distance between cloud centers of S/D = 1.2; that is, for cloud diameter of 1 km, there are gaps between the clouds of 0.2 km (Fig. 9). For the same cloud cover and cloud diameter, cylinders have a separation distance of S/D = 1.05; that is, the minimum gap between clouds is 0.05 km. Now consider the diagonal distance between the clouds shown in Fig. 9. For cubes, this distance is 0.28 km and for cylinders, 0.48 km, or about twice as far.

First, for aspect ratio H/D = 1, zenith angle $\theta_0 = 0°$ and cloud cover N = 0.7, cubes and cylinders produce nearly identical zenith angle scattering patterns for photons initially exiting the cloud (Fig. 10A, First Exit). These are the scattering patterns associated with non-interacting clouds. About 33%-34% of incident energy is scattered out the cloud tops and about 2% is transmitted out the cloud bases. Of the 65% of incident energy scattered out the cloud sides, about half exits

in the upper quarter of the cloud; only about 2% exits from the lower quarter of the cloud sides. Of the total energy out the cloud sides, about 25% is scattered into the upper hemisphere, and about 39%-40% scattered into the lower hemisphere. At zenith angle of $\theta_0 = 60°$ (Fig. 10B, First Exit), cylinders scatter a smaller proportion of incident energy out the cloud tops than do cubes; however, cylinders scatter more energy than cubes out the cloud sides. This is due to the fact that cylinders have a smaller average path length through the cloud at $\theta_0 > 0°$ than do cubes.

For $\theta_0 = 0°$, Fig. 10A (Final Exit) shows the photon scattering pattern on final exit from the cloud. This is the energy distribution after all cloud-cloud interactions have taken place. Note that a large redistribution of energy occurs through the cloud-cloud interactions. The percentage of incident energy scattered out the cloud sides drops from about 65% for photons first exiting the cloud to about 26% for photons on final exit from cubic clouds. Cylinders scatter a much larger percentage, about 35%-36%, out their sides. The result is that cubes scatter more energy out their tops and bases than do cylinders. A similar condition applies at zenith angles of $\theta_0 = 60°$ (Fig. 10B, Final Exit).

Consideration of these differences between cubes and cylinders provides an explanation of how the shape of holes between clouds may play an important role in cloud reflected fluxes. First, the scattering pattern on "First Exit" shows that photons travel more frequently in the downward than upward direction. Second, the majority of photons exiting

from the cloud sides leave from the upper quarter. Finally, the angular distribution pattern for photons out the cloud sides is anisotropic, with few photons exiting at zenith angles of 0°-30° and 150°-180°.

Perhaps most striking is the small number of photons on final exit from the cubes in the angular bin 90°-120°, and the large number of photons exiting in the angular bin 30°-60°. This is due to the fact that the majority of photons exit from the upper quarter of the cloud side. Those photons traveling in the 30°-60° angular bin more easily avoid further cloud-cloud interactions, whereas photons in the 120°-150° angular bin almost never avoid entering a neighboring cloud. In contrast, the relatively large gaps between clouds for the cylinders lead both to greater scattering from the clouds' sides and to a more symmetrical distribution of scattered photons. However, in all cases the scattering pattern remains highly anisotropic, with few photons in the 0°-30° and 150°-180° angular bins.

These angular patterns demonstrate that photons exiting cloud sides require considerable distance between neighbors in order to escape interaction with them. Since the greatest distance between clouds at N = 0.7 is about 0.3 km for cubes, and about 0.5 km for cylinders, many more photons are able to penetrate the cloud gaps without interaction from cylinders than from cubes. The result is that cylinders reflect less total incident energy for equal values of sky cover than do cubes.

As aspect ratio increases, cloud width decreases for clouds of equal vertical extent; cloud separation distance then decreases for

constant values of sky cover N. If the angular exitance pattern were invariant with aspect ratio, then increased interactions would make clouds of larger aspect ratio brighter. However, this is not the case. Increased numbers of photons exit the cloud sides as aspect ratio increases, and exit angles become more strongly peaked in the downward direction. These considerations more than compensate for the decrease in cloud separation, thereby reducing cloud reflectance for both cubes and cylinders as aspect ratio increases.

This analysis shows that the size of gaps between clouds strongly influences the total energy reflected by a cloud field at constant sky cover N. Choice of the hexagonal cloud pattern, rather than the linear array used above, decreases the average gap distance between cylindrically shaped clouds. The result is a brighter cloud field for the same cloud cover.

Close examination of Fig. 7 shows a number of examples of the hexagonal cloud array. Gaps between clouds also tend to be cusp-shaped, indicative of convex shaped clouds; linear patterns would indicate clouds with straight sides. As cloud cover N is increased towards N = 1, the clouds must become progressively deformed in order for $F_{cf}(1)$ to approach the plane-parallel limit $F_{pp}(1)$. Examination of the LANDSAT image in Fig. 7 indicates that clouds seldom are exactly circular in shape and almost never are cubic. Therefore, results between those for cubes and cylinders may be more appropriate.

e. Clouds with hemispherical tops

While most clouds are neither cylindrical nor cubic in shape, they also seldom have the flat cloud tops assumed in the previous results. The purpose of this section is to examine the effect of clouds having tops with the hemispherical shape. Aspect ratio is held constant with a value of H/D = 1 for these cases.

At $\theta_0 = 0°$, the value of $F_{cf}(N)/F_{pp}(N)$ for hemispheres (Fig. 11a) is similar to that for cylinders with aspect ratio H/D = 1/2. For capped cylinders (H/D = 1), values of $F_{cf}(N)/F_{pp}(N)$ increase more rapidly than do cylinders (H/D = 1). However, due to the much smaller values of effective area (Fig. A1) at $\theta_0 = 60°$, capped cylinders and hemispheres are significantly darker than their cylindrical or cubic counterparts at the same value of cloud cover N. Differences are largest at the small values of cloud cover. Shading limits occur at N = 0.14 for capped cylinders and N = 0.35 for hemispheres

At $\theta_0 = 0°$, capped cylinders have values of ΔF (Fig. 11b) which are smaller than for cylinders, but larger than for cubes. These values of ΔF are nearly identical to those of cylinders with the small aspect ratio H/D = 1/2.

At $\theta_0 = 60°$, the presence of curved cloud tops tends to minimize differences between plane-parallel and broken cloudiness.

4. Discussion

Enhanced values of reflected flux at solar zenith angle of 60° are largely due to geometrical effects. As shown by the ratio $N_e/N = F_{cf}(N)/F_{pp}(N)$, effective cloud cover N_e becomes much larger than actual cloud cover N. An attempt to correct for these geometrical effects can be made by redefining ΔF as

$$\Delta F' = F_{cf}(N) - F_{pp}(N') \quad , \tag{23}$$

where N' is an adjusted cloud cover. Taking $N' = A_C(\theta)/A$ as defined in Appendix A, $\Delta F'$ becomes

$$\Delta F' = [F_{cf}(N)/F_{pp}(N) - N'/N]\, NR_{pp}\, [F_o\mu_o(1-R_R)-A_b] \tag{24}$$

Figure 12 shows the values of $\Delta F'$ for solar zenith angle of 60°. Comparison of Figs. 5b and 8b with Fig. 12 shows that the values of $\Delta F'$ are negative and as large in magnitude as the values of ΔF. This suggests that an average between ΔF and $\Delta F'$ may be more accurate. Therefore, the empirical relationship

$$\Delta F'' = [F_{cf}(N)/F_{pp}(N) - (1+N'/N)/2]\, NR_{pp}\, [F_o\mu_o(1-R_R)-A_b] \tag{25}$$

is applied and is shown in Fig. 11. This kind of empirical fit also has been suggested by Harshvardhan and Thomas (1984). For cubes and cylinders, the value of $\Delta F''$ is negative at small values of cloud cover and positive at larger values of N. However, the magnitude of $\Delta F''$ is less than 15 W m^{-2} for cylinders and less than 10 W m^{-2} for cubes. For capped cylinders and hemispheres, the value of ΔF remains negative for

all values of cloud cover. The magnitude of ΔF is less than 10 W m^{-2} for capped cylinders and less than about 17 W m^{-2} for hemispheres. Therefore, the empirical fitting procedure allows for a relatively accurate method of obtaining cloud field reflected fluxes from plane-parallel calculations at solar zenith angle of 60°.

A caution is in order, lest the reader believe that a reliable method has been developed to calculate cloud field reflected fluxes. The accuracy of the $\Delta F''$ fit is limited to solar zenith angles near 60° and has not been established at cloud optical depths other than t = 49. Note that at solar zenith angle of 0°, N' = N, so that no improvement in the results is possible using the empirical method. As solar zenith angle is decreased from 60°, the error in $\Delta F''$ using the empirical fit must steadily increase (not shown in the figures).

5. Conclusions

The present study has been careful to preserve cloud liquid water volume as cloud shape was varied. It is assumed that cloud optical volume scales linearly with liquid water volume. In this way, the results give the differences in solar reflected fluxes which would be predicted for a cloud field with specified cloud fraction and cloud liquid water volume but varying cloud geometry. In particular, cloud fields with plane-parallel, cubic, cylindrical, hemispheric, and hemispherical-capped-cylinder geometries are compared for a range of cloud cover.

Values of $F_{cf}(N)/F_{pp}(N)$ shown in the figures give the scale factors which relate the albedos of broken cloudiness to the more familiar

plane-parallel values. At $\theta_0 = 0°$, the albedos of broken cloud fields are distinctly smaller than corresponding plane-parallel values; at $\theta_0 = 60°$, the broken cloud field albedos are larger, with maximum differences occurring at the shadowing limit.

However, perhaps of greater significance is the magnitude of the reflected flux differences between broken and plane-parallel cloudiness. For fixed solar zenith angle, the value of 10 W m^{-2} is used here as an estimate of "significant differences," chosen on the basis of detectability by broad-band flux measurements. This limit of $\Delta F < 10$ W m^{-2} occurs for $N < 0.1$ and for $N > 0.9$, indicating that plane-parallel calculations are not satisfactory at most values of sky cover.

For the larger values of sky cover, differences in ΔF can become very large for some cloud shapes. This is due to the fact that the scale factor $F_{cf}(N)/F_{pp}(N)$ is relatively "flat" as a function of N at $\theta_0 = 0°$ for convex-shaped clouds and does not approach the plane-parallel limit as $N \to 1$. Deformation from this circular cross section occurs in real clouds (Fig. 7), indicating that cloud albedos in between those predicted for cubes and cylinders may be more appropriate. The presence of convex cloud tops also serves to decrease the difference between plane-parallel and broken clouds and between cubes and cylinders. The net result is that cloud computations based upon cubic and rectangular geometries may provide reasonable estimations of cloud field albedo, at least in selected cases, even though real clouds do not have these geometries. Such agreement also is suggested by the observations of McKee et al. (1983).

In any case, the present results show that cloud shape and the size of the gaps between clouds are important variables. Clouds have an anisotropic intensity pattern out their sides and elongated cusp-like regions between clouds are efficient at allowing photons to propagate to the ground without interaction with neighboring clouds. Therefore, the presence of small holes, as opposed to long thin lines, between clouds may have a large impact upon cloud albedo. At large values of sky cover, these gaps may tend to act as "light pipes" in increasing cloud transmissivity and decreasing cloud albedo, producing results significantly different from those predicted by plane-parallel models.

At solar zenith angle of 60°, geometrical effects dominate, since effective cloud cover becomes much larger than actual cloud cover. An empirical relationship for effective cloud fraction was found to produce errors in ΔF less than 10 W m^{-2} for cubes and capped cylinders and less than about 15 W m^{-2} for cylinders and hemispheres. This technique, based upon a similar procedure by Harshvardhan and Thomas (1984), allows for the relatively accurate computation of broken cloud field reflected fluxes from plane-parallel calculations. However, the use of this empirical relationship is limited, since as solar zenith angle decreases from 60°, the error in ΔF using this relationship increases. At solar zenith angle of 0°, effective cloud fraction becomes cloud cover N.

Acknowledgments. This research was conducted under NASA/Langley Research Center computers. Thanks are extended to Dr. B. Barkstrom for constructive suggestions concerning this manuscript. Comments concerning effective cloud fraction by an anonymous reviewer are appreciated.

REFERENCES

Aida, M., 1976: Scattering of solar radiation as a function of cloud dimensions and orientation. J. Quant. Spectrosc. Radiat. Transfer, 17, 303-311.

_____, 1977: Reflection of solar radiation from an array of cumuli. J. Meteor. Soc. Japan, 55, 174-181.

Barkstrom, B. R., and J. B. Hall, Jr., 1982: Earth Radiation Budget Experiment (ERBE): An overview. J. of Energy , 6, 141-146.

Blackmer, R. H., and S. M. Serebreny, 1962: Dimensions and distributions of cumulus clouds as shown by U-2 photographs. Air Force Cambridge Research Labs, AFCRL-62-609. 47 pp.

Bradley, S. G., 1981: The relation between cumulus albedo and extinction coefficient and its application to remote sensing. J. Atmos. Sci., 38, 2243-2256.

Busygin, V. P., N. A. Yevstratov and E. M. Feigelson, 1973: Optical properties of cumulus and radiant fluxes for cumulus cloud cover. Izv. Atmos. Ocean Phys., 9, 1142-1151.

Claussen, M., 1982: On the radiative interaction in three-dimensional cloud fields. Contrib. Atmos. Phys., 55, 158-169.

Davies, R., 1978: The effect of finite geometry on the three-dimensional transfer of solar irradiance in clouds. J. Atmos. Sci., 35, 1712-1725.

Davis, J. M., S. K. Cox and T. B. McKee, 1979: Vertical and horizontal distributions of solar absorption in finite clouds. J. Atmos. Sci., 36, 1976-1984.

Donner, L. J., H. L. Kuo and E. J. Pitcher, 1982: The significance of thermodynamic forcing by cumulus convection in a general circulation model. J. Atmos. Sci., 39, 2159-2181.

Fouquart, Y., and B. Bonnel, 1980: Computations of solar heating of the earth's atmosphere: A new parameterization. Beitr. Phys. Atmosph., 53, 35-62.

Geleyn, J. F., A. Hense and H. J. Preuss, 1982: A comparison of model generated radiation fields with satellite measurements. Beitr. Phys. Atmosph., 55, 253-286.

_____, and A. Hollingsworth, 1979: An economical analytical method for the computation of the interaction between scattering and line absorption of radiation. Beitr. Phys. Atmosph., 52, 1-16.

Gube, M., J. Schmetz and E. Raschke, 1980: Solar radiative transfer in a cloud field. Contrib. Atmos. Phys., 53, 24-34.

Hahn, C. J., S. G. Warren, L. Londau, R. M. Chervin and R. Jenne, 1982: Atlas of simultaneous occurrence of different cloud types over the ocean. NCAR Technical Note, NCAR/TN-201. 212 pp.

Harshvardhan, 1982: The effect of brokenness on cloud-climate sensitivity. J. Atmos. Sci., 39, 1853-1861.

_____, and R. W. L. Thomas, 1984: Solar reflection from interacting and shadowing cloud elements. [Accepted by J. Geophys. Res.]

Hense, A., M. Kerschgens and E. Raschke, 1982: An economical method for computing radiative energy transfer in circulation models. Quart. J. Roy. Met. Soc., 108, 231-252.

Hozumi, K., T. Harimaya and C. Magono, 1982: The size distribution of cumulus clouds as a function of cloud amount. J. Meteor. Soc. Japan, 60, 691-699.

Kasahara, A., and W. M. Washington, 1971: General circulation experiments with a six-layer NCAR model, including orography, cloudiness and surface temperature calculations. J. Atmos. Sci., 28, 657-701.

Lacis, A. A., and J. E. Hansen, 1974: A parameterization for the absorption or solar radiation in the Earth's atmosphere. J. Atmos. Sci., 31, 118-133.

Marchuk, G. I., G. A. Mikhailov, M. A. Nazaraliev, R. A. Dorbinjan, B. A. Kargin and B. S. Elepov, 1980: The Monte Carlo Methods in Atmospheric Optics. New York: Springer-Verlag. 208 pp.

McClatchey, R. A., R. W. Fenn, J. E. Selby, F. E. Volz and J. S. Garing, 1971: Optical properties of the atmosphere. Environ. Res. Pap. No. 354, AFCRL.

McKee, T. B., and S. K. Cox, 1974: Scattering of visible radiation by finite clouds. J. Atmos. Sci., 31, 1885-1892.

_____, M. DeMaria, J. A. Kuenning and S. K. Cox, 1983: Comparison of Monte Carlo calculations with observations of light scattering in clouds. J. Atmos. Sci., 40, 1016-1023.

North, G. R., R. F. Cahalan and J. A. Coakley, Jr., 1981: Energy balance climate models. Rev. of Geophys. and Space Phys., 19, 91-121.

Plank, V., 1969: The size distribution of cumulus clouds in representative Florida populations. J. Appl. Meteor., 8, 46-67.

Ramanathan, V., E. J. Pitcher, R. C. Malone and M. L. Blackman, 1983: The response of a spectral general circulation model to refinements in radiative processes. J. Atmos. Sci., 40, 605-630.

Rossow, W. B., F. Mosher, E. Kinsella, A. Arking, M. Debois, E. F. Harrison, P. Minnis, E. Ruprecht, G. Seze, C. Simmer and E. Smith, 1984: ISCCP cloud analysis algorithm. WMO Publication (in press).

Slingo, J. M., 1980: A cloud parameterization scheme derived from GATE data for use with a numerical model. Quart. J. R. Met. Soc., 106, 747-770.

Sparrow, E. M., and R. D. Cess, 1978: Radiation Heat Transfer. New York: McGraw Hill. 366 pp.

Weinman, J. A., and Harshvardhan, 1982: Solar reflection from a regular array of horizontally finite clouds. Appl. Opt., 21, 2940-2944.

Welch, R. M., J. E. Geleyn, W. Zdunkowski and G. Korb, 1976: Radiative transfer of solar radiation in model clouds. Contrib. Atmos. Phys., 49, 128-146.

Welch, R. M., and W. G. Zdunkowski, 1981a: The radiative characteristics of non-interacting cumulus cloud fields, Part I: Parameterization of finite clouds. Contrib. Atmos. Phys., 54, 258-273.

_____, and _____, 1981b: The radiative characteristics of non-interacting cumulus cloud fields, Part II: Calculations for cloud fields. Contrib. Atmos. Phys., 54, 274-286.

Wiscombe, W. J., R. M. Welch and W. D. Hall, 1984: The effects of very large drops on cloud absorption. I. Parcel models. J. Atmos. Sci., 41, --.

Zdunkowski, W. G., W. G. Panhaus, R. M. Welch and G. N. Korb, 1982: A radiation scheme for circulation and climate models. Contrib. Atmos. Phys., 55, 215-237.

APPENDIX A

The value N_e is defined as the equivalent cloud fraction of a plane-parallel cloud of the same vertical optical thickness (horizontally averaged over the cloud field) which produces the same flux as from the finite cloud array,

$$F_{cf} = N_e F_{pp} \tag{A1}$$

where the plane-parallel flux is expressed as

$$F_{pp} = R_{pp} \mu_o F_o \quad . \tag{A2}$$

Plane-parallel albedo is R_{pp}, F_o is incident solar flux, and μ_o is the cosine of the solar zenith angle θ_o. Flux from the cloud field array is given by

$$F_{cf}(N) = R_{cf} \mu_o F_o \quad , \tag{A3}$$

where cloud field albedo R_{cf} is

$$R_{cf} = R_c A_C(N,\theta_o)/A \quad , \tag{A4}$$

taking ground albedo as zero. Cloud albedo R_c is the fraction of photons intercepted by the cloud (top and sides) that are reflected back to space, $A_C(N,\theta_o)$ is the projection of cloud area onto a horizontal surface as viewed from the solar direction, and $A=S^2$ is the total area of a unit cell surrounding the cloud.

Cubic clouds. For cubic clouds of thickness H and width D, cloud intercepted area is

$$A_C(N,\theta_o) = \begin{cases} D^2 + DH \tan\theta_o, & [S/D > 1 + H/D \tan\theta_o] \\ DS, & [S/D < 1 + H/D \tan\theta_o, \text{ shading}]. \end{cases} \quad (A5)$$

Combining Eqs. (A4) and (A5), cloud field albedo becomes

$$R_{cf} = \begin{cases} R_c N (1 + H/D \tan\theta_o), & [S/D > 1 + H/D \tan\theta_o] \\ R_c N^{1/2}, & [S/D < 1 + H/D \tan\theta_o, \text{ shading}]. \end{cases} \quad (A6)$$

Scaling the plane-parallel flux (Eq. A2) by cloud cover N produces

$$F_{pp}(N) = N F_{pp} \quad . \quad (A7)$$

Finally, combining Eqs. (A1-A7), we obtain the albedo enhancement factor (or effective cloud fraction ratio):

$$F_{cf}(N)/F_{pp}(N) = N_e/N = R_c R_{pp}^{-1} \begin{cases} (1 + H/D \tan\theta_o), & [\text{no shading}] \\ N^{-1/2}, & [\text{shading}]. \end{cases} \quad (A8)$$

This is the amount by which cloud field reflectance is increased above or decreased below the equivalent plane-parallel value, $F_{pp}(N)$.

Cylindrical clouds. For cylindrically shaped clouds, unshaded area is given by

$$A_C(N,\theta_o) = \pi D^2/4 + DH \tan\theta_o, \quad [S/D > 1 + H/D \tan\theta_o] \quad (A9)$$

Partially shaded area is given by

$$A_C(N,\theta_o) = \begin{cases} DS, \text{ for } [S/D < H/D \tan\theta_o] \\ DH \tan\theta_o + D^2/D \sin^{-1}(S/D - H/D \tan\theta_o) \\ + (S - H \tan\theta_o)/2[D^2 - (S - H \tan\theta_o)^2]^{1/2}, \\ \text{for } [H/D \tan\theta_o < S/D < 1 + H/D \tan\theta_o] \quad . \end{cases} \tag{A10}$$

Combining the above expressions leads to the albedo enhancement factor for cylindrically shaped clouds:

$$F_{cf}(N)/F_{pp}(N) = R_c R_{pp}^{-1} \begin{cases} (1 + 4/\pi\ H/D \tan\theta_o), \text{ for } [S/D > 1 + H/D \tan\theta_o] \\ 4/\pi[H/D \tan\theta_o + 1/2 \sin^{-1}(S/D - H/D \tan\theta_o) \\ + (S/D - H/D \tan\theta_o)/2(1-(S/D - H/D \tan\theta_o)^2)^{1/2}], \\ \text{for } [H/D \tan\theta_o < S/D < 1 + H/D \tan\theta_o] \\ 4/\pi\ S/D \text{ for } [S/D < H/D \tan\theta_o] \quad . \end{cases} \tag{A11}$$

Capped cylinders and hemispheres. For capped cylinders (SPHCYL) and for hemispherically shaped clouds (SPH), the albedo enhancement factor is more mathematically complicated. Therefore, it is given here in the form

$$F_{cf}(N)F_{pp}(N) = R_c R_{pp}^{-1}[A_C(N,\theta_o)[A_C(N,0°)] \tag{A12}$$

where area enhancement factors, $A_C(N,60°)/A_C(N,0°)$, are shown in Fig. A1 as a function of N for each cloud shape.

APPENDIX B

The results presented previously express cloud field radiative fluxes in terms of plane parallel values. These computations are proportioned to cloud field area enhancement values (e.g., Fig. A1) and to the ratio of interacting to non-interacting cloud field reflectance values. Let values R and R_1 represent cloud reflectance values for interacting and non-interacting clouds, respectively; then ratio R/R_1 is the reflectance enhancement factor representing the effect of photons, exiting from one cloud, which enter a neighboring cloud. Reflectance enhancement ratios are given in Fig. B1 for cloud fields composed of cubes, cylinders, and hemispherically topped clouds, respectively.

Reflectance ratios for cubic clouds at solar zenith angles of $\theta_0 = 0°$ and 60° are shown in Fig. B1(a,b). These values increase with increasing value of cloud cover. For complete cloud cover (N = 1), cloud interactions increase cloud albedo 27%, above that which would be found for completely non-interacting clouds. These values are nearly identical to values reported by Aida (1977) and Weinman and Harshvardhan (1982). For aspect ratios of H/D = 2 and 1/2, maximum increase in cloud albedo is 57% and 12%, respectively, over that produced by non-interacting cloud fields. Clearly, cloud aspect ratio is a variable of great importance to cloud field albedo.

At $\theta_0 = 60°$, cloud interactions enhance cloud albedo by 44%, 67%, and 89% for H/D = 1/2, 1, and 2, respectively. The discontinuity in values shown in Fig. B1(b) occurs at the cloud mutual shading limit.

Figure B1(c,d) shows corresponding values for cylinders. Albedo enhancement ratio at $\theta_0 = 0°$ is considerably smaller for all aspect ratios than corresponding values of cubes. Differences are due to the fact that photons existing from cloud sides have less chance of interacting with cylindrically shaped clouds than with cubic shaped clouds. Maximum sky cover is N = 0.79 for the checkerboard array and N = 0.91 for the hexagonal array. Note that only the single case of aspect ratio unity is shown for the hexagonal array (HEX). At $\theta_0 = 60°$, values of R/R_1 for cylinders are similar to those values for cubes, indicating again tnat shadowing is a dominant influence on values of cloud field albedo.

Figure B1(e,f) shows similar values of R/R_1 for hemispheres and capped cylinders. Cloud extinction coefficients are adjusted from $\beta_e = 49$ km^{-1} to values of $\beta_e = 73$ km^{-1} and 59 km^{-1} for hemispheres and capped cylinders, respectively, so as to preserve cloud optical volume. Capped cylinders have larger values of R/R_1 at $\theta_0 = 0°$ than do the flat-topped cylinders. In contrast, hemispheres produce values of R/R_1 similar to those for cylinders with aspect ratio H/D = 1/2.

At $\theta_0 = 60°$, both capped cylinders and hemispheres have values of R/R_1 significantly smaller than those produced by cylinders. These differences are associated with shading effects produced by the curved upper surfaces.

FIGURE CAPTIONS

Fig. 1: Cloud field array composed of cubic shaped clouds of diameter (width) D with cloud spacing S. Paths of three photons are shown which interact with neighboring clouds; primes indicate the reinsertion points for these photons with the original cloud.

Fig. 2: The four cloud geometries used in this investigation are shown here.

Fig. 3: Cloud field arrays for convex shaped clouds of diameter D with cloud spacing S, arrayed in A) linear and B) hexagonal patterns.

Fig. 4: Shading by neighbors for A) cubic shaped clouds; and B) cylindrically shaped clouds.

Fig. 5: A) Ratio of cubic cloud field radiative fluxes to plane-parallel fluxes as a function of cloud cover; B) The difference between cubic cloud field and plane-parallel radiative fluxes in W m^{-2} as a function of cloud cover.

Fig. 6: Comparison of present and previous results at $\theta_0 = 0°$ for cloud field radiative fluxes. A) Ratio of cubic cloud field radiative fluxes to plane-parallel fluxes as a function of cloud cover; B) The difference between cubic cloud field and plane-parallel radiative fluxes as a function of cloud cover.

Fig. 7: LANDSAT Multispectral Scanner (MSS) image with 80 m resolution taken off the coast of southern California on 23 September 1979. Horizontal scale is 185 km and vertical scale is 170 km.

Fig. 8: A) Ratio of cylindrical cloud field radiative fluxes scaled to plane-parallel fluxes as a function of cloud cover; B) The difference between cylindrical cloud field and plane-parallel radiative fluxes in W m^{-2} as a function of cloud cover. "HEX" refers to cylinders (H/D = 1) arrayed in the hexagonal pattern (Fig. 3b).

Fig. 9: Sizes (in km) of the gaps between clouds (at N = 0.7) for cloud fields composed of cubes and cylinders.

Fig. 10: The angular distribution of radiation out the cloud sides at N = 0.7 for cubes and cylinders at solar zenith angles of A) θ_0 = 0° and B) 60°. The angular pattern is divided into segments each 30° in zenith angle width. The concentric circles represent exiting energy of 5%, 10%, 15%, 20%, and 25% of total incident energy for photons first exiting the cloud, and 2% 4%, 6%, and 8% of total incident energy for photons finally exiting the cloud (including cloud-cloud interactions). The boxes to the left of each half-circle show the percentage of total incident energy which exits each quarter of the cloud sides, from top to bottom.

Fig. 11: A) Ratio of cloud field radiative fluxes scaled to plane-parallel fluxes as a function of cloud cover for capped cylinders and hemispheres; B) The difference between cloud field and plane-parallel radiative fluxes as a function of cloud cover.

Fig. 12: The difference between cloud field and plane-parallel radiative fluxes as a function of cloud cover calculated on the basis of the A) $\Delta F'$; and B) $\Delta F''$ approximations.

Fig. A1: Area enhancement ratios as a function of cloud cover N for the four cloud shapes shown in Fig. 2. Cloud aspect ratio is H/D = 1. "HEX" refers to cylindrically shaped clouds arrayed in the hexagonal pattern (Fig. 3b).

Fig. B1: Reflectance enhancement factors as a function of sky cover at solar zenith angles $\theta_0 = 0°$ and 60° for (a,b) cubes; (c,d) cylinders; (e,f) capped cylinders and hemispheres.

TABLE 1

S/D	CUBIC CLOUDS	CONVEX-SHAPED CLOUDS Square Array	CONVEX-SHAPED CLOUDS Hexagonal Array
1.00	100.0	78.5	90.7
1.05	91.0	71.0	82.2
1.10	82.0	65.0	75.0
1.20	70.0	54.5	63.0
1.50	45.0	35.0	40.3
2.00	25.0	20.0	22.7
3.00	11.0	8.5	10.0
4.00	6.0	5.0	5.7

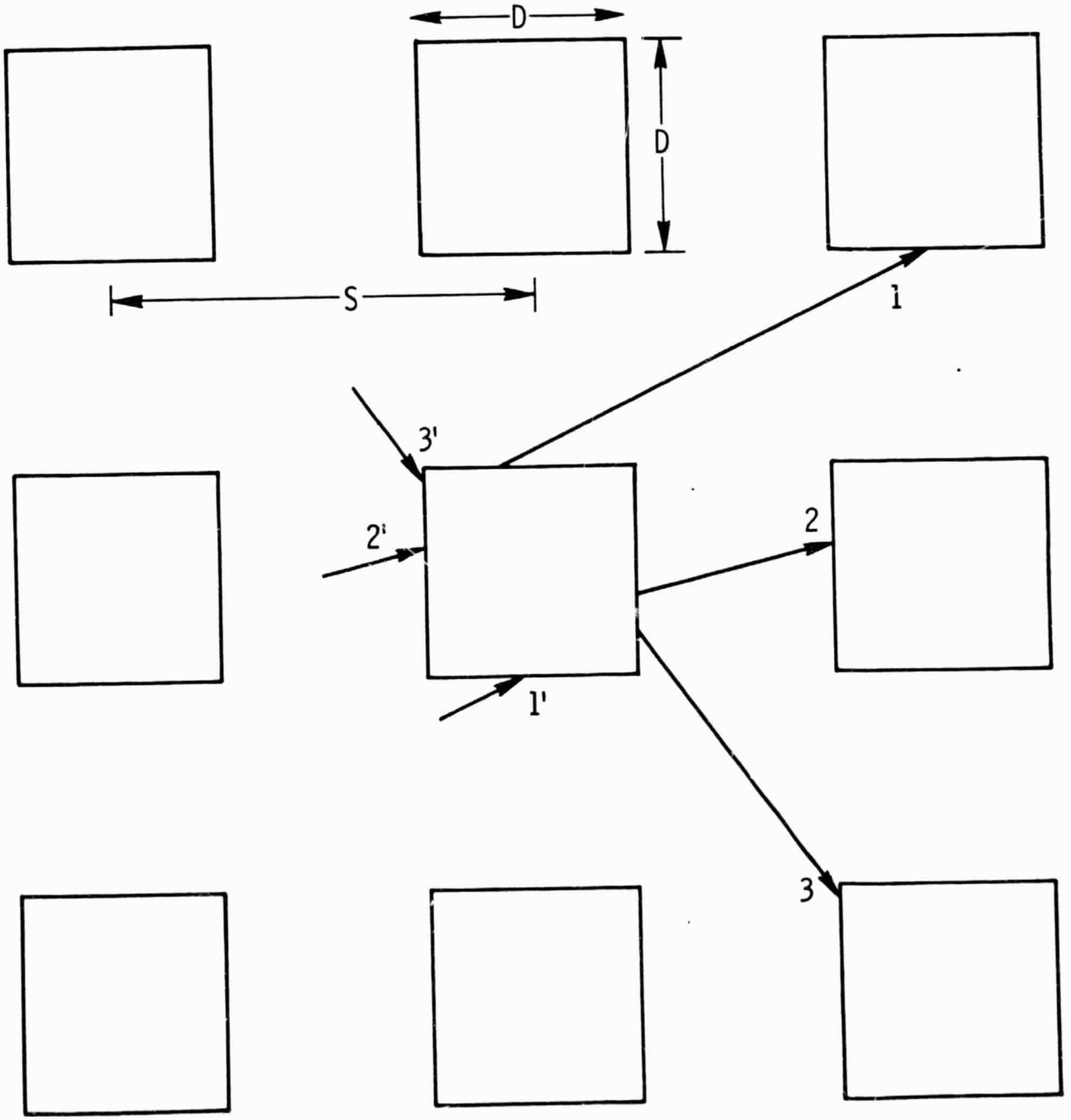

FIG 1

CLOUD GEOMETRIES

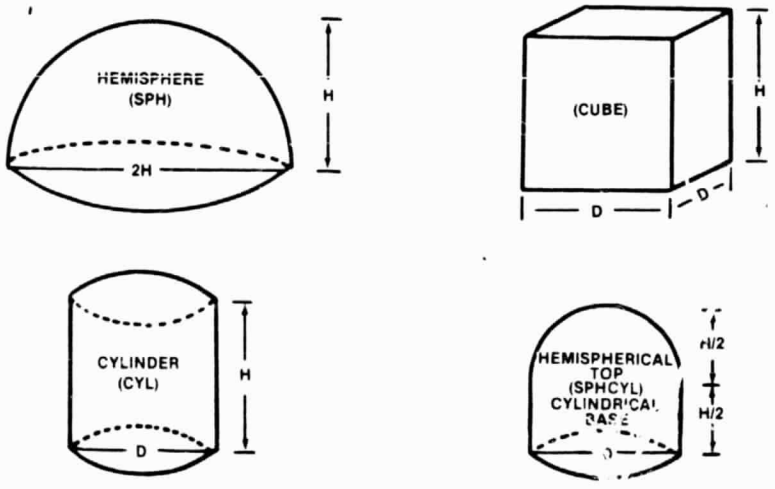

FIG 2

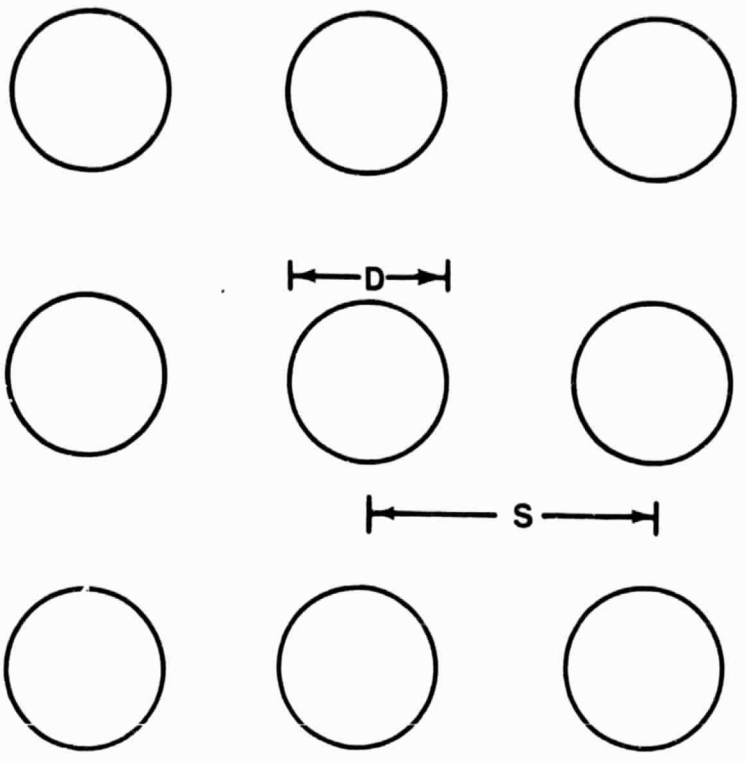

(A)

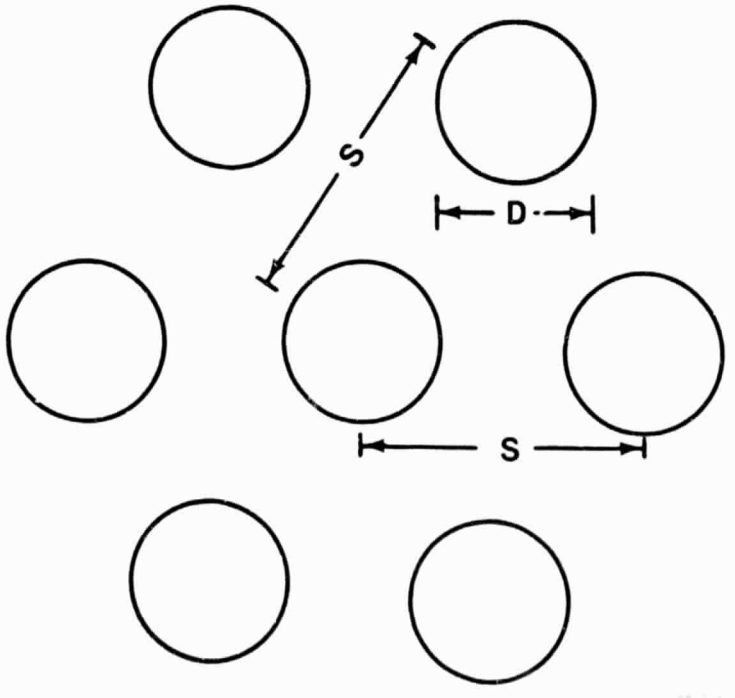

(B)

FIG 3

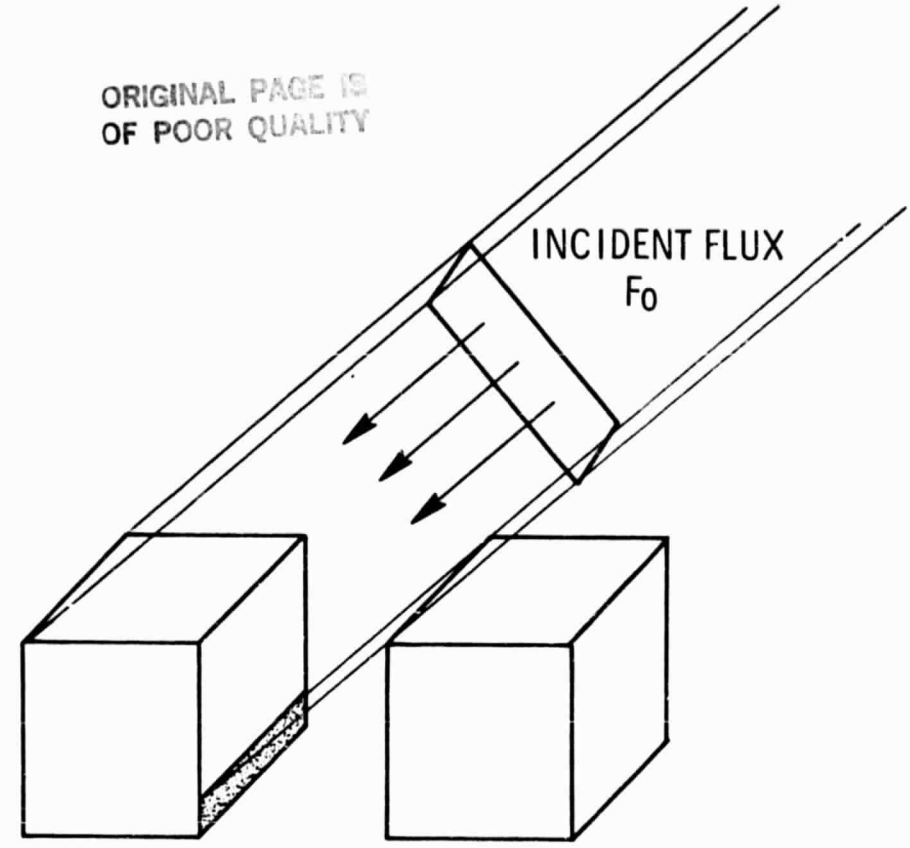

(A)

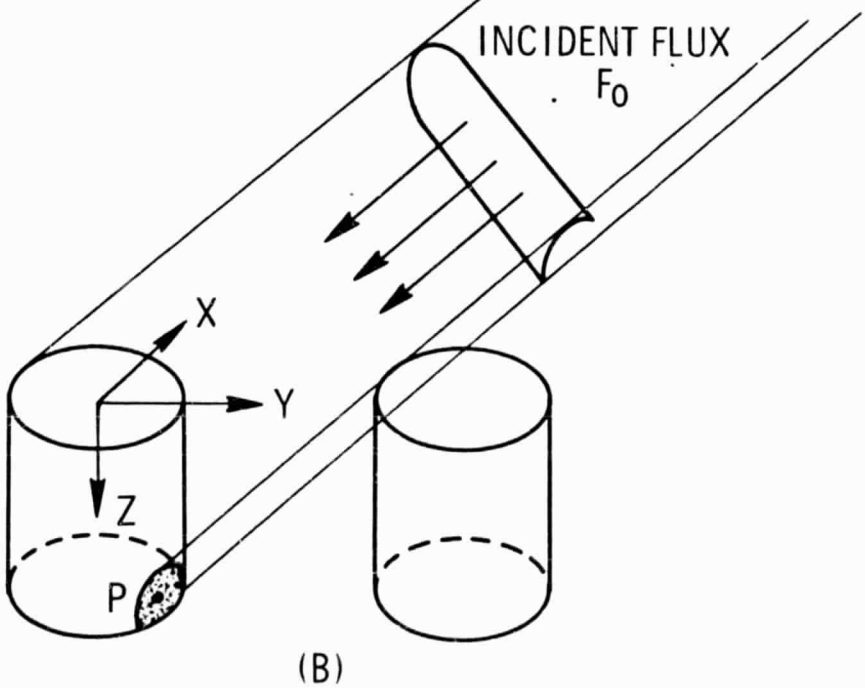

(B)

FIG 4

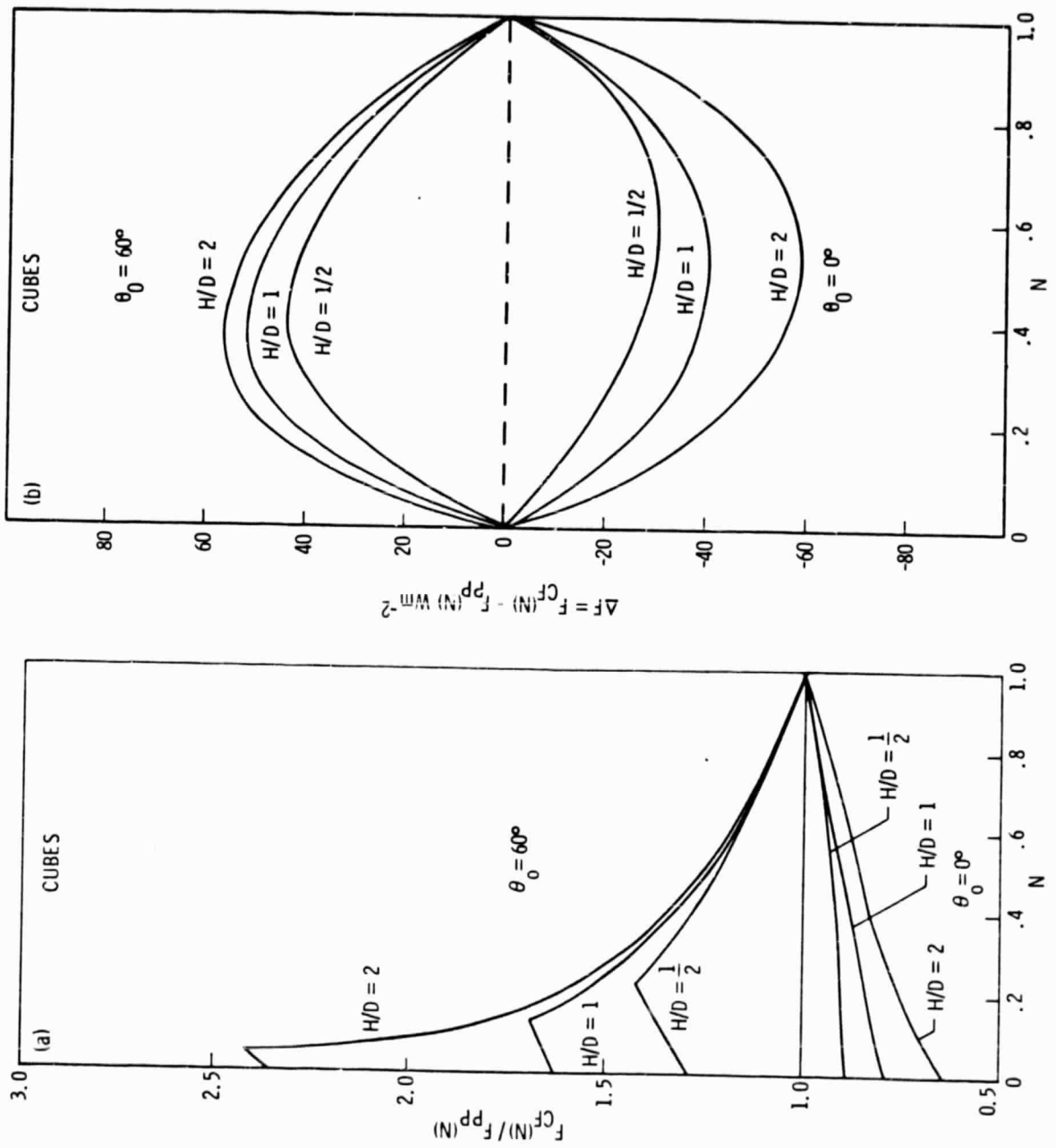

FIG 5

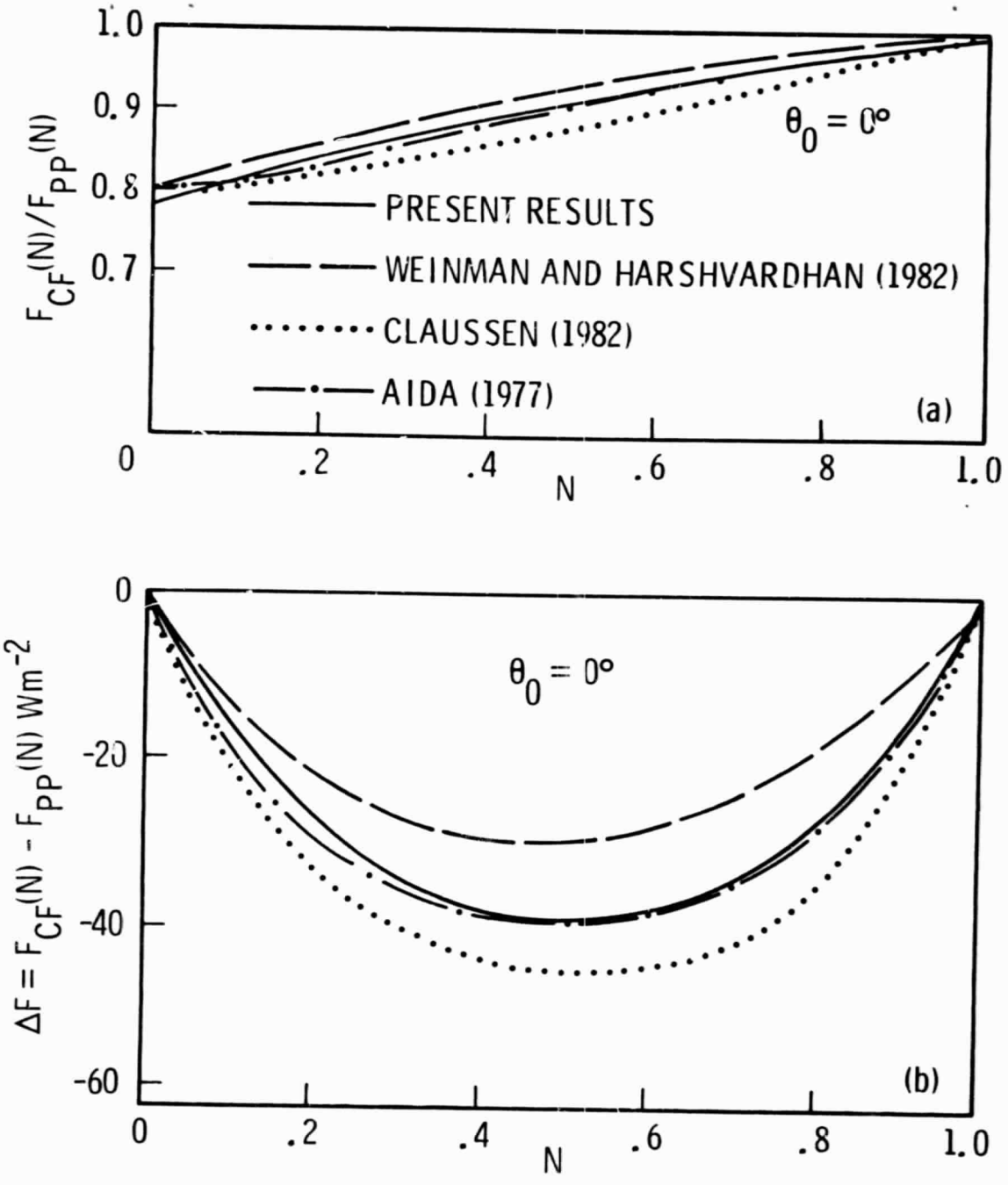

FIG 6

00639-118

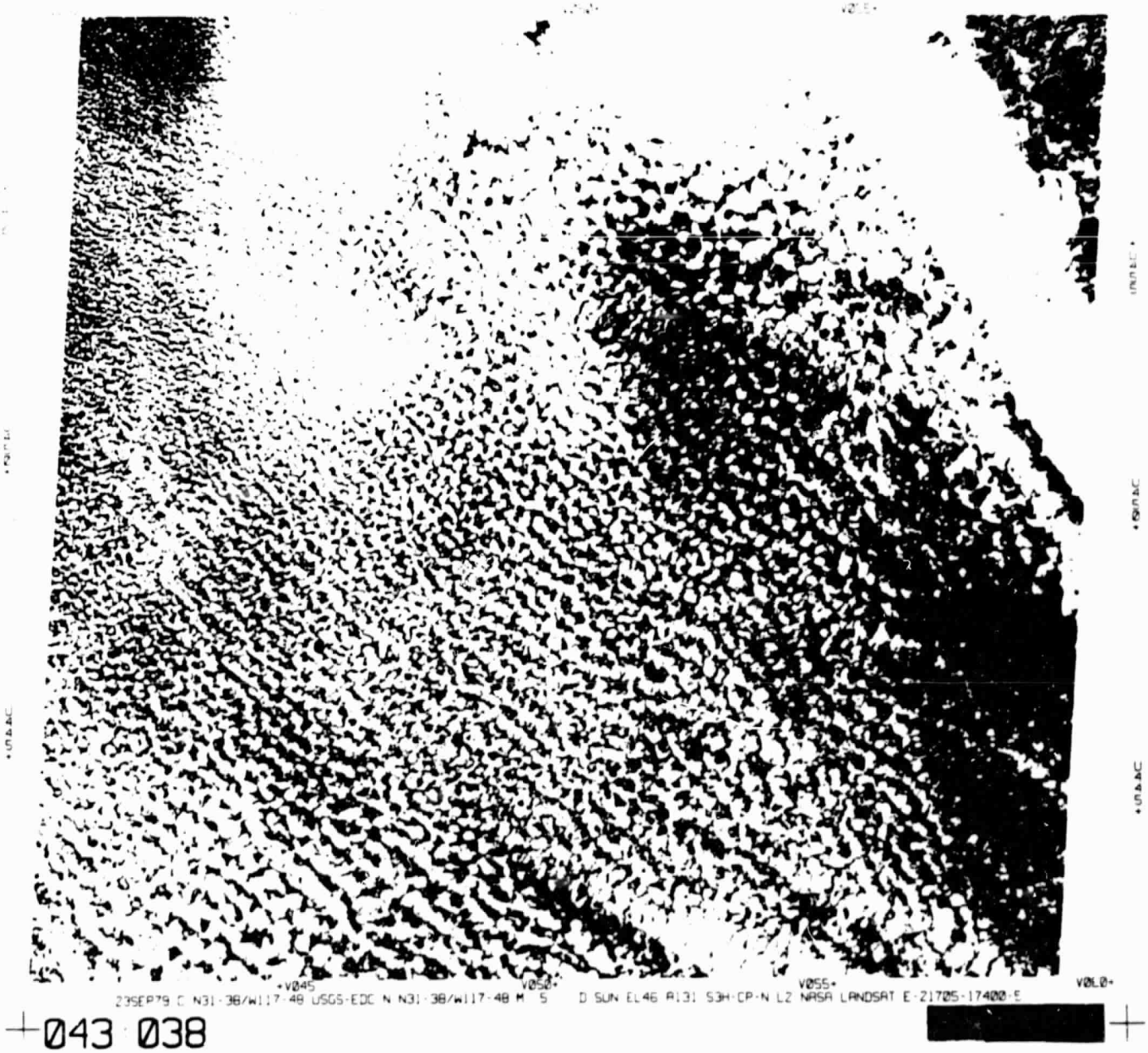

043 038

FIG 7

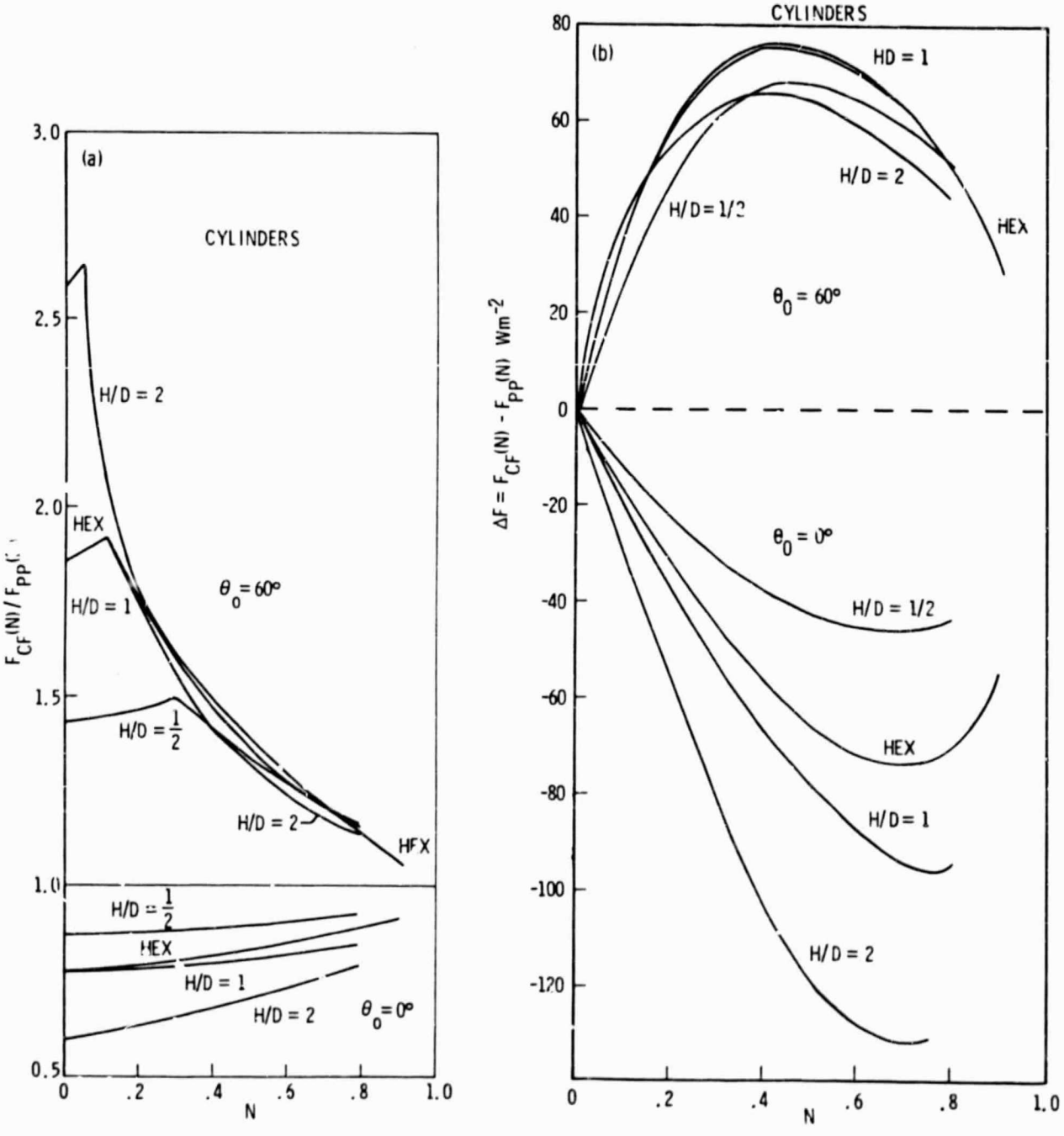

FIG 8

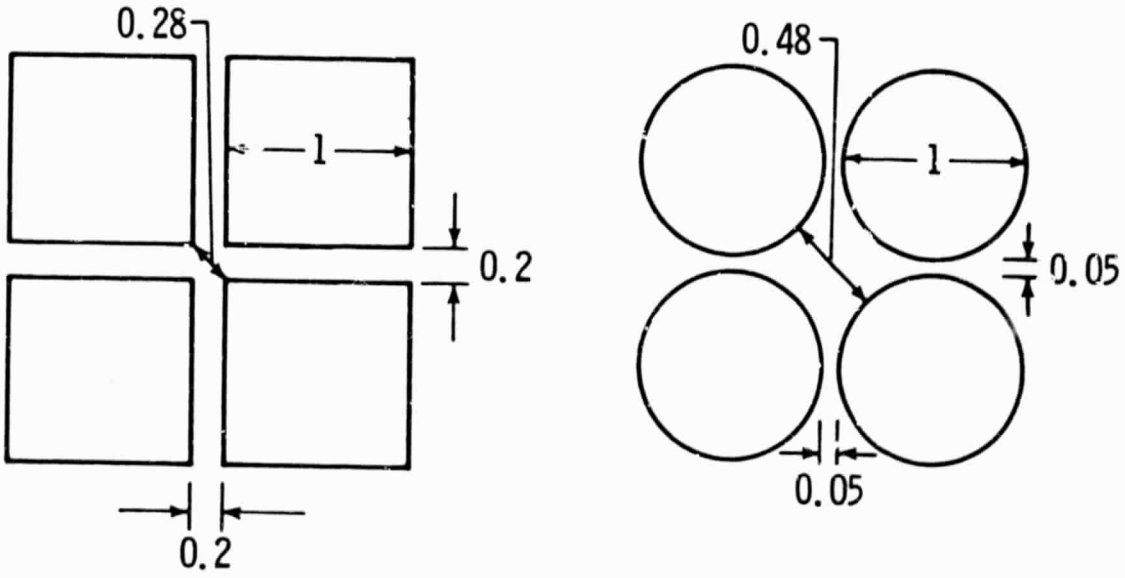

N = 0.7

FIG 9

(a) $\theta_0 = 0°$

FIRST EXIT

CUBES

TOP 34.59

37.14

17.16

6.61

2.10

BOT 2.39

25%
20%
15%
10%
5%

UP
24.84

DOWN
38.18

CYLINDERS

TOP 33.05

38.44

18.01

6.39

2.00

BOT 2.11

UP
25.11

DOWN
39.73

FINAL EXIT

CUBES

TOP 57.10

14.59

3.51

2.67

5.18

BOT 16.94

8%
6%
4%
2%

UP
15.94

DOWN
10.02

CYLINDERS

TOP 50.29

16.91

8.70

5.86

4.92

BOT 13.33

UP
17.65

DOWN
18.73

FIG 10A

(b) $\theta_0 = 60°$

FIRST EXIT

CUBES

TOP 45.48

36.88

10.69

4.24

1.40

BOT 1.32

25%
20%
15%
10%
5%

UP
18.44

DOWN
34.76

CYLINDERS

TOP 42.01

40.31

11.61

3.77

1.20

BOT 1.09

UP
19.41

DOWN
37.48

FINAL EXIT

CUBES

TOP 64.62

12.91

2.69

1.99

4.83

BOT 12.95

8%
6%
4%
2%

UP
14.43

DOWN
8.00

CYLINDERS

TOP 57.93

16.18

7.32

4.71

3.51

BOT 10.34

UP
15.45

DOWN
16.27

FIG 10B

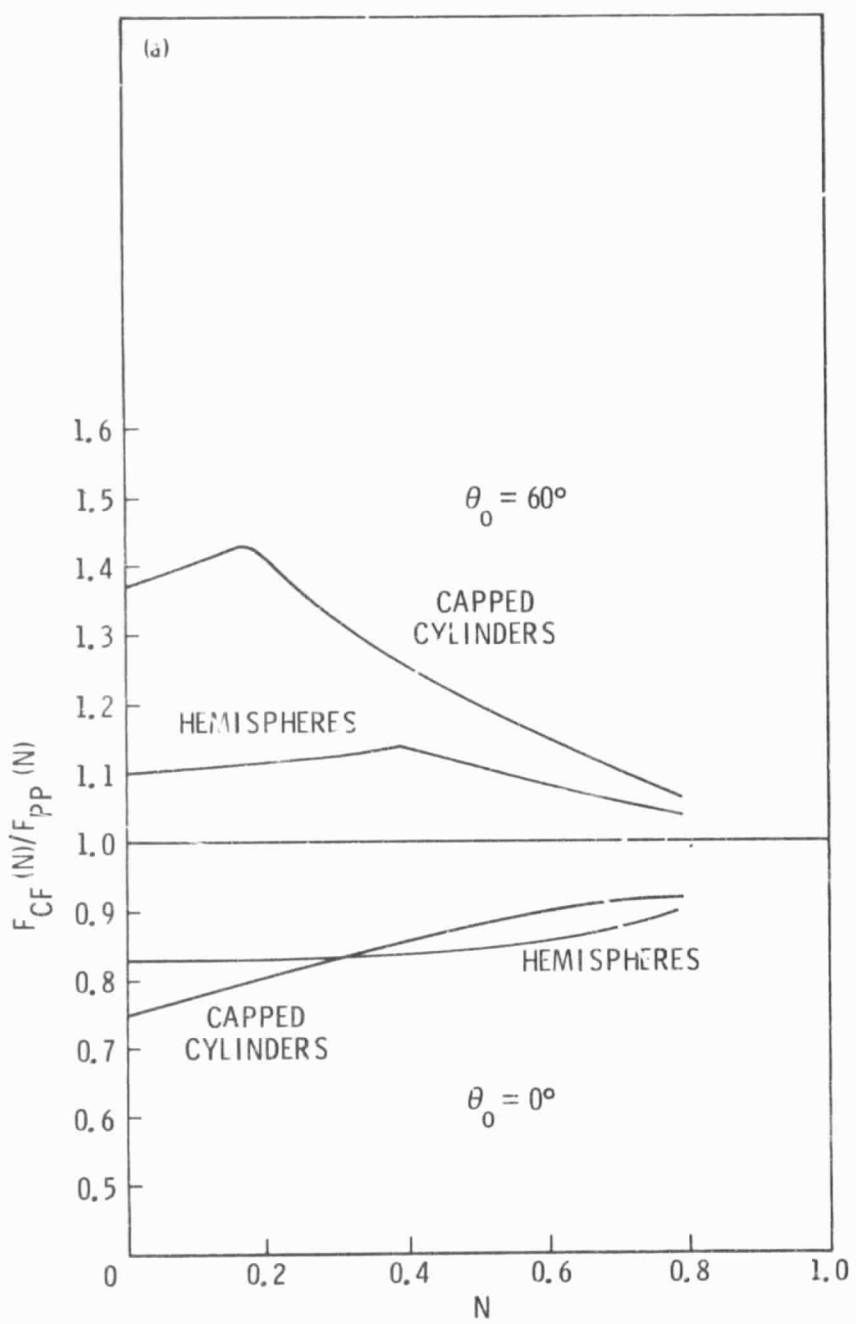

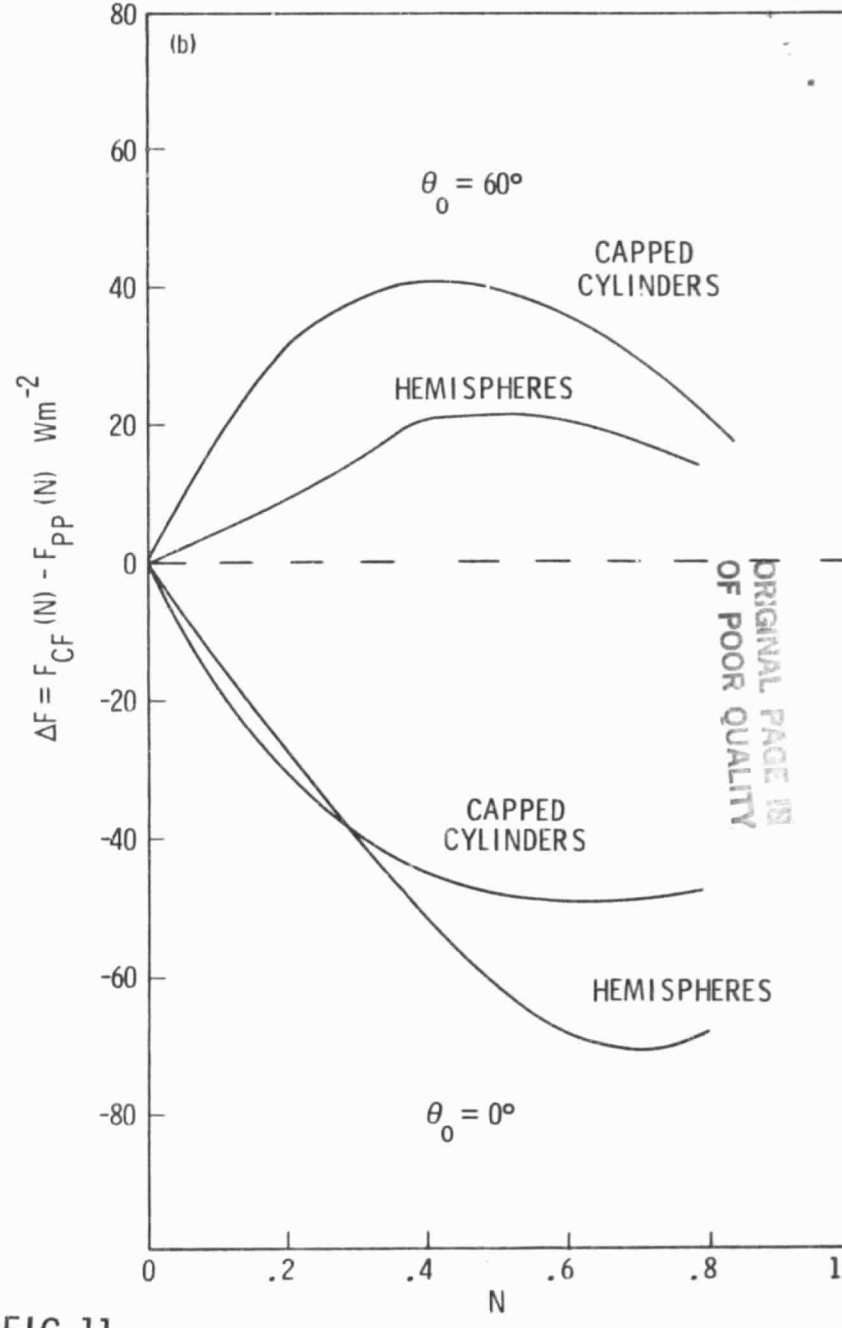

FIG 11

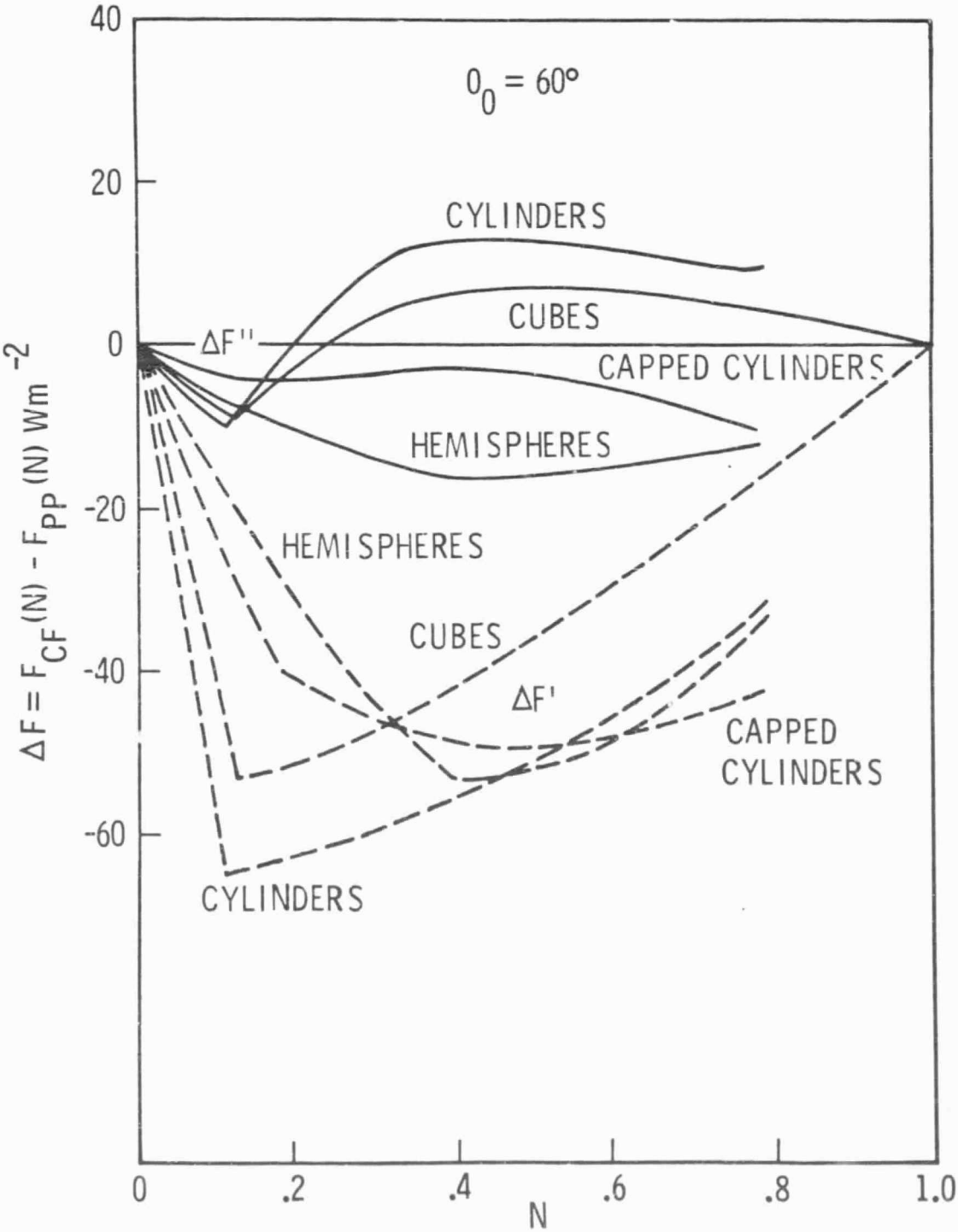

FIG 12

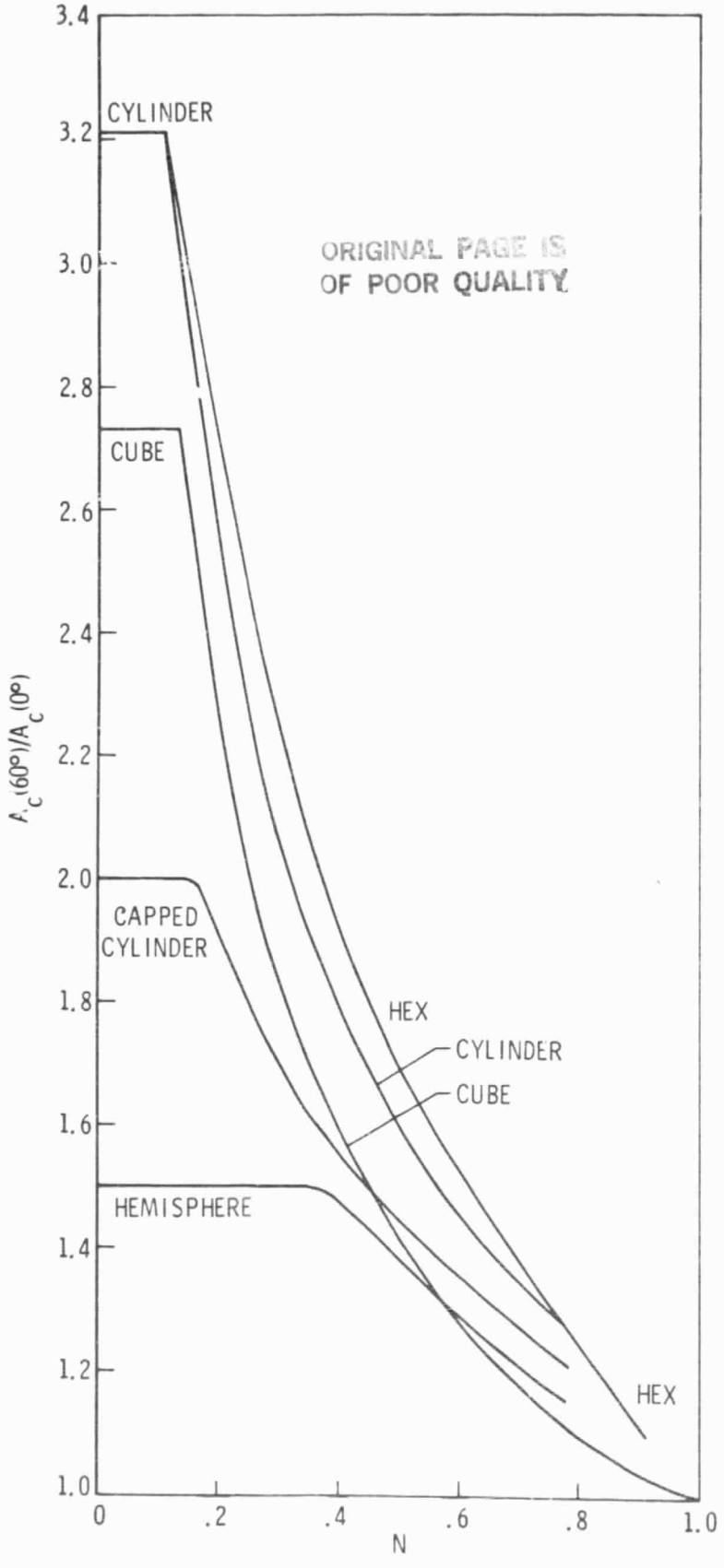
3.4
3.2
3.0
2.8
2.6
2.4
2.2
2.0
1.8
1.6
1.4
1.2
1.0
0
.2
.4
.6
.8
1.0
N
$A_c(60°)/A_c(0°)$
CYLINDER
CUBE
CAPPED CYLINDER
HEMISPHERE
HEX
CYLINDER
CUBE
HEX
ORIGINAL PAGE IS
OF POOR QUALITY

FIG A1

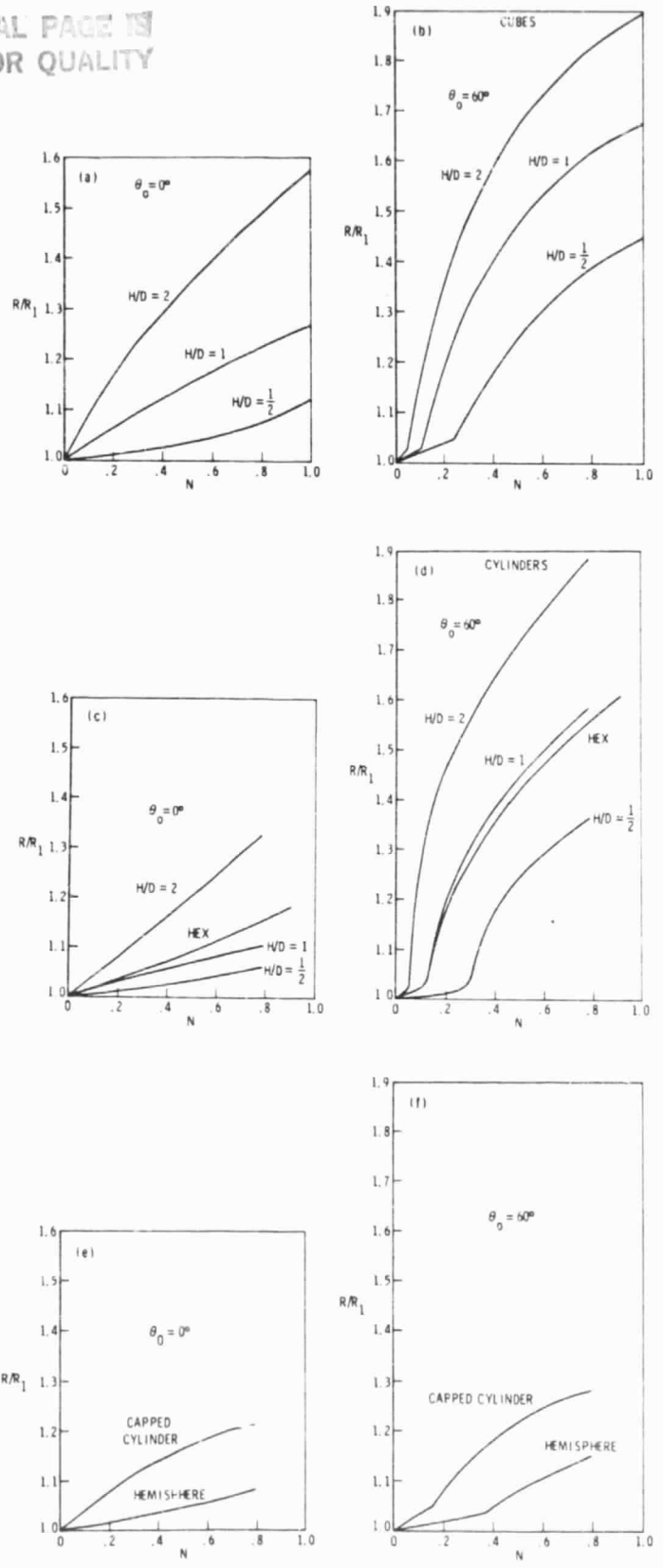

FIG B1